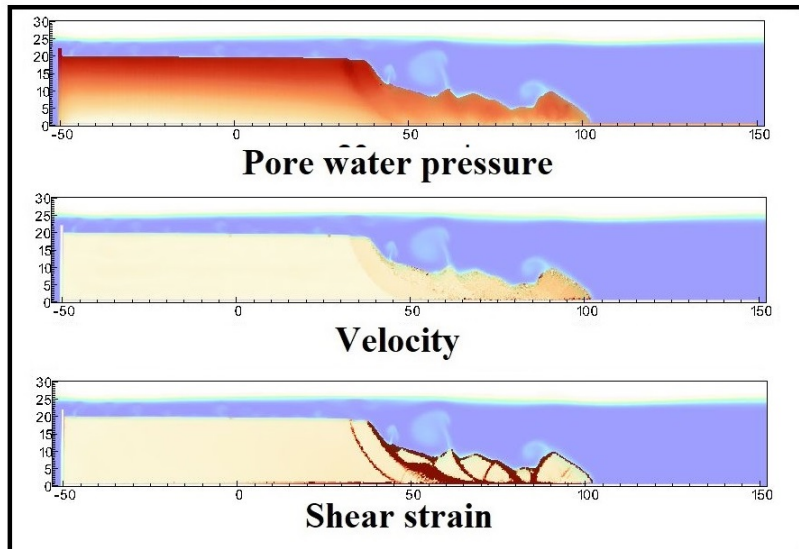


- 1 Graphical Abstract
- 2 MPMICE: A hybrid MPM-CFD model for simulating coupled problems in porous media. Application to earthquake-induced submarine landslides
- 3 Quoc Anh Tran, Gustav Grimstad, Seyed Ali Ghoreishian Amiri



Application to earthquake-induced submarine landslide

₆ Highlights

₇ **MPMICE: A hybrid MPM-CFD model for simulating coupled prob-**
₈ **lems in porous media. Application to earthquake-induced subma-**
₉ **rine landslides**

₁₀ Quoc Anh Tran, Gustav Grimstad, Seyed Ali Ghoreishian Amiri

- ₁₁ • MPMICE is introduced for multiphase flow in porous media.
- ₁₂ • Material Point method allows to model large deformation of non-isothermal
- ₁₃ porous media.
- ₁₄ • ICE (compressible multi-material CFD formulation) allows stabilizing
- ₁₅ pore water pressure and turbulent flow.
- ₁₆ • MPMICE is validated and apply to simulate the earthquake-induced
- ₁₇ submarine landslide.

¹⁸ MPMICE: A hybrid MPM-CFD model for simulating
¹⁹ coupled problems in porous media. Application to
²⁰ earthquake-induced submarine landslides

²¹ Quoc Anh Tran^{a,b}, Gustav Grimstad^a, Seyed Ali Ghoreishian Amiri^a

^a*Norwegian University of Science and Technology, , Trondheim, 7034, Norway*
^b*quoc.a.tran@ntnu.no*

²² **Abstract**

²³ In this paper, we describe a soil-fluid-structure interaction model that com-
²⁴ bines soil mechanics (saturated sediments), fluid mechanics (seawater or air),
²⁵ and solid mechanics (structures). The formulation combines the Material
²⁶ Point Method, which models large deformation of the porous media and the
²⁷ structure, with the Implicit Continuous-fluid Eulerian, which models com-
²⁸ plex fluid flows. We validate the model and simulate the whole process of
²⁹ earthquake-induced submarine landslides. We show that this model captures
³⁰ complex interactions between saturated sediment, seawater, and structure,
³¹ so we can use the model to estimate the impact of potential submarine land-
³² slides on offshore structures.

³³ *Keywords:*

³⁴ Material Point Method, MPMICE, submarine landslide.

35	Contents	
36	Nomenclature	4
37	Introduction	6
38	Theory and formulation	9
39	Assumptions	9
40	Governing equations	9
41	Constitutive soil model	11
42	Turbulent model	12
43	Frictional force for soil-structure interaction	13
44	Momentum and Energy exchange model	13
45	Solving momentum and energy exchange with an implicit solver	15
46	Equation of state for fluid phases	16
47	Numerical implementation	17
48	Interpolation from Solid Particle to Grid	18
49	Compute equation of state for fluid phase	20
50	Compute cell face velocity	20
51	Compute cell face temperature	21
52	Compute fluid pressure (implicit scheme)	22
53	Compute viscous shear stress term of the fluid phase	22
54	Compute nodal internal temperature of the solid phase	23
55	Compute and integrate acceleration of the solid phase	23
56	Compute Lagrangian value (mass, momentum and energy)	23
57	Compute Lagrangian specific volume of the fluid phase	25
58	Compute advection term and advance in time	25
59	Interpolate from cell to node of the solid phase	26
60	Update the particle variables	26
61	Numerical validation	27
62	Fluid Flow through isothermal porous media	27
63	Isothermal consolidation	28
64	Thermal induced cavity flow	29
65	Numerical examples	31
66	Underwater debris flow	31
67	Validation of soil response to the seismic loading	34

68	Earthquake-induced submarine landslides	37
69	Conclusions	42
70	Acknowledgements	43
71	Appendix: Equation derivation	43
72	Evolution of porosity	43
73	Momentum conservation	44
74	Energy conservation	45
75	Advanced Fluid Pressure	46
76	Momentum and Energy exchange with an implicit solver	47

⁷⁷ **Nomenclature**

General variables

<u>Variable</u>	<u>Dimensions</u>	<u>Description</u>
V	$[L^3]$	Representative volume
n		Porosity
σ	$[ML^{-1}t^{-2}]$	Total stress tensor
Δt	$[t]$	Time increment
\mathbf{b}	$[ML^1t^{-2}]$	Body force
c_v	$[L^2t^{-2}T^{-1}]$	Constant volume specific heat
f_d	$[MLt^{-2}]$	Drag forces in momentum exchange term
f^{int}	$[MLt^{-2}]$	Internal forces
f^{ext}	$[MLt^{-2}]$	External forces
q_{fs}	$[MLt^{-2}]$	Heat exchange term
S		Weighting function
∇S		Gradient of weighting function

⁷⁸

Solid phase

<u>Variable</u>	<u>Dimensions</u>	<u>Description</u>
m_s	$[M]$	Solid mass
ρ_s	$[ML^{-3}]$	Solid density
ϕ_s		Solid volume fraction
$\bar{\rho}_s$	$[ML^{-3}]$	Bulk Solid density
\mathbf{x}_s	$[L]$	Solid Position vector
\mathbf{U}_s	$[Lt^{-1}]$	Solid Velocity vector
\mathbf{a}_s	$[Lt^{-2}]$	Solid Acceleration vector
σ'	$[ML^{-1}t^{-2}]$	Effective Stress tensor
ϵ		Strain tensor
e_s	$[L^2t^{-2}]$	Solid Internal energy per unit mass
T_s	$[T]$	Solid Temperature
\mathbf{F}_s		Solid Deformation gradient
V_s	$[L^3]$	Solid Volume

Fluid phase

<u>Variable</u>	<u>Dimensions</u>	<u>Description</u>
m_f	[M]	Fluid mass
ρ_f	[ML ⁻³]	Fluid density
ϕ_f		Fluid volume fraction
$\bar{\rho}_f$	[ML ⁻³]	Bulk Fluid density
\mathbf{U}_f	[Lt ⁻¹]	Fluid Velocity vector
$\boldsymbol{\sigma}_f$	[ML ⁻¹ t ⁻²]	Fluid stress tensor
p_f	[ML ⁻¹ t ⁻²]	Fluid isotropic pressure
$\boldsymbol{\tau}_f$	[ML ⁻¹ t ⁻²]	Fluid shear stress tensor
e_f	[L ² t ⁻²]	Fluid Internal energy per unit mass
T_f	[T]	Fluid Temperature
v_f	[L ³ /M]	Fluid Specific volume $\frac{1}{\rho_f}$
α_f	[1/T]	Thermal expansion
μ	[ML ⁻¹ t ⁻¹]	Fluid viscosity
V_f	[L ³]	Fluid Volume

Superscript

<u>Variable</u>	<u>Dimensions</u>	<u>Description</u>
n		Current time step
L		Lagrangian values
$n + 1$		Next time step

Subscript

c	Cell-centered quantity
p	Particle quantity
i	Node quantity
FC	Cell face quantity
L, R	Left and Right cell faces

80 **Introduction**

81 Many geological natural processes and their interactions with man-made
82 structures are influenced by soil-fluid-structure interactions. The prediction
83 of these processes requires a tool that can capture complex interactions
84 between soil, fluid, and structure, such as the process of submarine land-
85 slides. Indeed, The offshore infrastructure as well as coastal communities
86 may be vulnerable to submarine landslides. Submarine landslides contain
87 three stages: triggering, failure, and post-failure. Erosion or earthquakes can
88 trigger slope failures in the first stage. Following the failure, sediments move
89 quickly after the post-failure stage. In other words, solid-like sediments will
90 behave like a fluid after failure. This transition, where the sediment trans-
91 forms into fluid-like debris and then re-establishes a porous medium, poses
92 a challenging task for simulating submarine landslides.

93 Due to this transition, submarine landslides can be modeled using either the
94 Eulerian framework or the Lagrangian framework. The Eulerian framework
95 involves the calculation of material response at specific time-space points.
96 For instance, methods within Computational Fluid Dynamics, for example
97 using Finite Volume Methods (FVM) are employed to simulate submarine
98 landslides [1, 2, 3, 4] by solving governing equations in a full-Eulerian frame-
99 work. While FVM is capable of handling complex flows, such as turbulent
100 flows, it falls short of accounting for the triggering mechanisms of subma-
101 rine landslides. This is due to the challenge of incorporating 'constitutive
102 laws' of sediment materials within the Eulerian framework. This is particu-
103 larly significant because converting material time derivatives into fixed space
104 derivatives involves arduous mathematical tasks, especially for soil materials
105 that rely on nonlinear tensor operations and history-dependent state/internal
106 variables. In contrast, the Lagrangian framework, including various particle-
107 based methods, provides a solution to this problem. In the Lagrangian frame-
108 work, material "particles" are tracked individually through space, and ma-
109 terial properties and internal variables are determined at and follow these
110 particles. These methods have been extensively used to simulate landslides,
111 like Material Point Method (MPM) [5], Smooth Particle Hydro Dynamics [6],
112 Particle Finite Element Method [7], or Coupled Eulerian-Lagrangian Method
113 [8]. For simplicity, these previous simulations have adopted a total stress
114 analysis, neglecting the pore pressure development which is a key factor trig-
115 gering slope failures.

116 Recent advancements in particle-based Lagrangian methods have allowed for

the modeling of fluid flows in porous media using sets of Lagrangian particles. Within the MPM family, there is a specific approach known as double-point MPM [9, 10, 11]. In this method, fluid particles and solid particles are overlaid within a single computational grid. However, it is important to note that particle-based methods encounter numerical instability when modeling fluid flows. To address this, various numerical techniques are employed, including the B-bar method [9], null-space filter [12], or least square approximation [13, 14]. These methods are necessary, especially when dealing with complex and turbulent fluid flows, such as those seen in submarine landslides. In such scenarios, Eulerian methods like FVM/CFD are preferred due to their computational efficiency, particularly when turbulence occurs at fine resolutions. CFD has even been employed in combination with the Discrete Element Method [15, 16] to study granular grain - fluid interactions, allowing for the examination of micro-scale behavior and realistic grain morphology. However, the computational demands of Discrete Element Methods can be quite challenging when applied to practical scenarios. Therefore, an ideal approach might involve the integration of CFD with particle-based continuum methods. Additionally, MPM can also be coupled with thermal effects [17, 18, 19], opening up the possibility of capturing hydro-thermal-mechanical coupling. Over the past two decades, more than 50 particle-based methods have been developed to address the simulation of large deformations in solids [20]. Among these, MPM emerges as a strong candidate for coupling with CFD. This is because MPM incorporates a stationary mesh during computation, just like CFD. As such, MPM and CFD can be seamlessly integrated within a unified computational mesh, offering a promising approach for tackling complex fluid-solid interactions.

A numerical method for simulating soil-fluid-structure interaction (Figure 1) involving large deformations, is presented in this work in order to simulate the interaction between sediment (soil), seawater (fluid) and offshore structures (structure) namely MPMICE (Figure 2). In the MPMICE, the Material Point Method (MPM) is coupled with the Implicit Continuous Eulerian (ICE) [21]. The MPM method is a particle method that allows the porous soil to undergo arbitrary distortions. The ICE method, on the other hand, is a conservative finite volume technique with all state variables located at the cell center (temperature, velocity, mass, pressure). The ICE method offers certain advantages in comparison to conventional FVM in the realm of flow computation encompassing all velocity ranges. An initial technical report [22] at Los Alamos National Laboratory provided the theoretical and

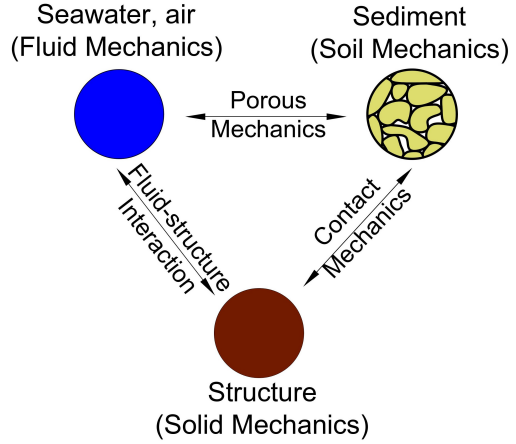


Figure 1: Interaction between soil-fluid-structure

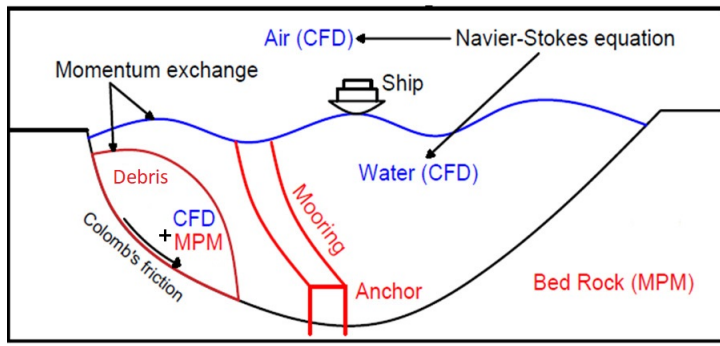


Figure 2: Coupling of soil-water-structure interaction using MPMICE

155 algorithmic foundation for the MPMICE, followed by the MPMICE development
 156 and implementation in the high-performance Uintah computational
 157 framework for simulating fluid-structure interactions [23]. This paper pri-
 158 marily contributes further to the development of the MPMICE for analyzing
 159 the **soil**-fluid-structure interaction, since sediment should be considered as a
 160 porous media (soil) and not as a solid to capture the evolution of the pore
 161 water pressure. Baumgarten et al. [24] made the first attempt at coupling
 162 the FVM with the MPM for the simulation of soil-fluid interaction by us-
 163 ing an explicit time integration for the single-phase flow. In contrast to the
 164 mentioned work, we use implicit time integration for the multi phase flows.

165 **Theory and formulation**

166 This section lay out the theoretical framework for the MPMICE model.
167 We use the common notation of the continuum mechanics with vector and
168 tensor denoted simply by using bold font and scalar denoted by using normal
169 font. The notation are shown in Nomenclature.

170 **Assumptions**

171 The following assumptions are made for the MPMICE model.

- 172 1. Solid phases (MPM) are described in a Lagrangian formulation while
173 fluid phases (ICE) are described in an Eulerian formulation in the
174 framework of continuum mechanics and mixture theory.
175 2. Solid grains are incompressible while the fluid phases are compressible.
176 3. There is no mass exchange between solid and fluid phases.
177 4. Terzaghi's effective stress is valid.

178 **Governing equations**

179 A representative element volume Ω is decomposed by two domains: solid
180 domains Ω_s and fluid domains Ω_f . Then, all domains are homogenized
181 into two overlapping continua. Considering the volume fraction of solid
182 $\phi_s = \Omega_s/\Omega$ and fluid $\phi_f = \Omega_f/\Omega$ with the true (or Eulerian) porosity
183 $n = \sum \phi_f$ of the representative element volume, the average density of solid
184 and fluid phases are defined as:

185

$$\bar{\rho}_s = \phi_s \rho_s, \quad \bar{\rho}_f = \phi_f \rho_f \quad (1)$$

186 The mass of solid and fluid phases are:

187

$$m_s = \int_{\Omega_s} \rho_s dV = \bar{\rho}_s V, \quad m_f = \int_{\Omega_f} \rho_f dV = \bar{\rho}_f V \quad (2)$$

188 Reviewing the Terzaghi's effective stress concept for the saturated porous
189 media, the total stress $\boldsymbol{\sigma}$ is calculated by:

190

$$\boldsymbol{\sigma} = \boldsymbol{\sigma}' - p_f \mathbf{I} \quad (3)$$

191 The balance equations are derived based on the mixture theory. The rep-
192 resentative thermodynamic state of the fluid phases are given by the vector
193 $[m_f, \mathbf{U}_f, e_f, T_f, v_f]$ which are mass, velocity, internal energy, temperature,

194 specific volume. The representative state of the solid phases are given by the
 195 vector $[m_s, \mathbf{U}_s, e_s, T_s, \boldsymbol{\sigma}', p_f]$ which are mass, velocity, internal energy, temper-
 196 ature, effective stress and pore water pressure. The derivation is presented
 197 in detail in the Appendix.

198

199 Mass Conservation

200 The mass balance equations for both fluid (e.g., water, air) and solid phases
 201 are:

202

$$\frac{1}{V} \frac{\partial m_f}{\partial t} + \nabla \cdot (m_f \mathbf{U}_f) = 0, \frac{1}{V} \frac{D_s m_s}{Dt} = 0 \quad (4)$$

203 Solving the mass balance equation of the solid phase leads to:

$$\frac{D_s n}{Dt} = \phi_s \nabla \cdot \mathbf{U}_s \quad (5)$$

204

205 Momentum Conservation

206 The momentum balance equations for each fluid phases (e.g., water, air) are:

$$\frac{1}{V} \left[\frac{\partial(m_f \mathbf{U}_f)}{\partial t} + \nabla \cdot (m_f \mathbf{U}_f \mathbf{U}_f) \right] = -\phi_f \nabla p_f + \nabla \cdot \boldsymbol{\tau}_f + \bar{\rho}_f \mathbf{b} + \sum \mathbf{f}_d \quad (6)$$

207 The momentum balance equations for each solid phases are:

$$\frac{1}{V} \frac{D_s(m_s \mathbf{U}_s)}{Dt} = \nabla \cdot (\boldsymbol{\sigma}') - \phi_s \nabla p_f + \bar{\rho}_s \mathbf{b} + \sum \mathbf{f}_{fric} - \sum \mathbf{f}_d \quad (7)$$

208

209 Energy Conservation

210 The internal energy balance equations for each fluid phases (e.g., water, air)
 211 are:

$$\frac{1}{V} \left[\frac{\partial(m_f e_f)}{\partial t} + \nabla \cdot (m_f e_f \mathbf{U}_f) \right] = -\bar{\rho}_f p_f \frac{D_f v_f}{Dt} + \boldsymbol{\tau}_f : \nabla \mathbf{U}_f + \nabla \cdot \mathbf{q}_f + \sum q_{sf} \quad (8)$$

212 The internal energy balance equations for each solid phases are:

$$\frac{m_s}{V} c_v \frac{D_s(T_s)}{Dt} = \boldsymbol{\sigma}' : \frac{D_s(\boldsymbol{\epsilon}_s^p)}{Dt} + \nabla \cdot \mathbf{q}_s - \sum q_{sf} \quad (9)$$

213 where c_v is the specific heat at constant volume of the solid materials.

214

215 Closing the systems of equations, the following additional models are needed:
 216 (1) A constitutive equation to describe the stress - strain behaviour of solid
 217 phase (computing effective stress σ').
 218 (2) Optional turbulent model to compute the viscous shear stress τ_f .
 219 (3) Frictional forces \mathbf{f}_{fric} for the contact for soil-structure interaction be-
 220 tween solid/porous materials with the friction coefficient μ_{fric} .
 221 (4) Exchange momentum models (computing drag force \mathbf{f}_d) for interaction
 222 between materials.
 223 (5) Energy exchange models (computing temerature exhange term q_{sf}) for
 224 interaction between materials.
 225 (6) An equation of state to establish relations between thermodynamics vari-
 226 ables of each fluid materials $[P_f, \bar{\rho}_f, v_f, T_f, e_f]$.
 227 (7) Thermal conduction model to compute thermal flux of solid phase \mathbf{q}_s and
 228 liquid phase \mathbf{q}_s .
 229 Four thermodynamic relations for the equation of states are:

$$\begin{aligned}
 e_f &= e_f(T_f, v_f) \\
 P_f &= P_f(T_f, v_f) \\
 \phi_f &= v_f \bar{\rho}_f \\
 0 &= n - \sum_{f=1}^{N_f} v_f \bar{\rho}_f
 \end{aligned} \tag{10}$$

230 *Constitutive soil model*

231 As a result of the explicit MPM formulation, we can derive the consti-
 232 tutive law in the updated Lagrangian framework of "small strain - large
 233 deformation". Therefore, the rotation of the particles (representative ele-
 234 ment volume) is manipulated by rotating the Cauchy stress tensor. First,
 235 the deformation gradient is decomposed into the polar rotation tensor \mathbf{R}_s^{n+1}
 236 and stretch tensor \mathbf{V}_s^{n+1} as:

$$\mathbf{F}_s^{n+1} = \mathbf{V}_s^{n+1} \mathbf{R}_s^{n+1} \tag{11}$$

237 Then, before calling the constitutive model, the stress and strain rate tensor
 238 are rotated to the reference configuration as:

$$\boldsymbol{\sigma}'^{n*} = (\mathbf{R}_s^{n+1})^T \boldsymbol{\sigma}'^n \mathbf{R}_s^{n+1} \tag{12}$$

$$\delta\boldsymbol{\epsilon}^{n*} = (\mathbf{R}_s^{n+1})^T \delta\boldsymbol{\epsilon}^n \mathbf{R}_s^{n+1} \tag{13}$$

240 Using the constitutive model with the input tensors $\sigma'^{n*}, \delta\epsilon^{n*}$ to compute
 241 the Cauchy stress tensor at the advanced time step σ'^{n+1*} then rotating it
 242 back to current configuration as:

$$\sigma'^{n+1} = R_s^{n+1} \sigma'^{n+1*} (R_s^{n+1})^T \quad (14)$$

243 In this paper, we adopt the hyper-elastic Neo Hookean model for the structure
 244 materials and additionally Mohr-Coulomb failure criteria for the soil (porous
 245 media) materials. The Cauchy stress of the hyper-elastic Neo Hookean model
 246 can be written as:

$$\sigma' = \frac{\lambda \ln(J)}{J} + \frac{\mu}{J} (\mathbf{F}\mathbf{F}^T - \mathbf{J}) \quad (15)$$

247 where λ and μ are bulk and shear modulus ad J is the determinant of the
 248 deformation gradient \mathbf{F} . And the yield function f and flow potentials g of
 249 the Mohr-Coulomb can be written as:

$$\begin{aligned} f &= -\sigma'_1 + \sigma'_3 + 2c' \cos(\phi') + (\sigma'_1 + \sigma'_3) \sin(\phi') \\ g &= -\sigma'_1 + \sigma'_3 + 2c' \cos(\psi') + (\sigma'_1 + \sigma'_3) \sin(\psi') \end{aligned} \quad (16)$$

250 In the equations, c' , ϕ' , and ψ' represent the cohesion, friction angle, and
 251 dilation angle, respectively. σ'_1 and σ'_3 denote the maximum and minimum
 252 principal stresses, with the condition $\sigma'_1 < \sigma'_3 < 0$. It is important to note
 253 that in our assumptions, stress is considered positive during extension, which
 254 means the signs of the stresses in these equations are opposite to those in
 255 standard Soil Mechanic's textbooks. The numerical implementation follows
 256 the approach described in Clausen et al. [25].

257 *Turbulent model*

258 The turbulent effect is modelled using a statistical approach namely large-
 259 eddy simulation. In this approach, the micro-scale turbulent influence in the
 260 dynamics of the macro-scale motion is computed through simple models like
 261 Smagorinsky model [26]. In the Smagorinsky model, the residual stress tensor
 262 is:

$$\tau_{ij} = 2\mu_{eff}(\bar{S}_{ij} - \frac{1}{3}\delta_{ij}\bar{S}_{kk}) + \frac{1}{3}\delta_{ij}\tau_{kk} \quad (17)$$

263 where the the strain rate tensor is given by:

$$\bar{S}_{ij} = \frac{1}{2}(\frac{\delta \bar{\mathbf{U}}_i}{\delta x_j} + \frac{\delta \bar{\mathbf{U}}_j}{\delta x_i}) \quad (18)$$

264 and the effective viscosity is sum of molecular viscosity and turbulent viscosity
 265 $\mu_{eff} = \mu + \mu_t$ in which the turbulent viscosity μ_t is calculated by:

$$\mu_t = (C_s \Delta)^2 \sqrt{2\bar{S}_{ij}\bar{S}_{ij}} \quad (19)$$

266 where C_s is the Smagorinsky constant with the value of 0.1 and $\Delta = \sqrt[3]{dxdydz}$
 267 is the grid size that defines the subgrid length scale.

268 *Frictional force for soil-structure interaction*

269 MPMICE includes a contact law for the interaction between soil and
 270 structure using the first Coulomb friction contact for MPM presented by
 271 Bardenhagen et al. [27]. The magnitude of the friction force at the contact
 272 depends on the friction coefficient μ_{fric} and the normal force \mathbf{f}_{norm} computed
 273 from the projection of the contact force in the normal direction.

$$\mathbf{f}_{fric} = \mu_{fric} \mathbf{f}_{norm} \quad (20)$$

274 The contact determines whether the soil is sliding or sticking to the structure
 275 by comparing the friction force with the sticking force \mathbf{f}_{stick} can be computed
 276 from the projection of the contact force in the tangent direction as:

$$\begin{aligned} & \text{if } \mathbf{f}_{fric} \geq \mathbf{f}_{stick} \text{ no sliding} \\ & \text{if } \mathbf{f}_{fric} < \mathbf{f}_{stick} \text{ sliding occurs} \end{aligned} \quad (21)$$

277 Frictional sliding between solid materials also generates dissipation and the
 278 work rate generated from the sliding can be calculated as:

$$\Delta W_{friction} = \mathbf{f}_{fric} d \quad (22)$$

279 where d is the sliding distance which can be computed based on the sliding
 280 velocity between two materials.

281 *Momentum and Energy exchange model*

282 Currently, the energy exchange coefficient H_{sf} is assumed to be constant
 283 for the sake of simplicity. Then the energy exchange can be written as:

$$q_{sf} = H_{sf}(T_f - T_s) \quad (23)$$

284 On the other hand, the drag force can be calculated as:

$$f_d = K(\mathbf{U}_s - \mathbf{U}_f) \quad (24)$$

285 For the momentum exchange between fluid flows and porous media, we as-
 286 sume that the drag force \mathbf{f}_d depends on the average grain size of the grains
 287 D_p , the porosity n , the fluid viscosity μ_f , and is proportional to the relative
 288 velocities of soil grains and fluid $(\mathbf{U}_s - \mathbf{U}_f)$. Based on recent investigation
 289 of CFD simulations of fluid flow around mono- and bi-disperse packing of
 290 spheres for $0.1 < \phi_s < 0.6$ and $Re < 1000$ [28]. The drag force is given by:
 291

$$\mathbf{f}_d = \frac{18\phi_s(1-\phi_s)\mu_f}{D_p^2} F(\phi_s, Re)(\mathbf{U}_s - \mathbf{U}_f) \quad (25)$$

292 where Reynolds number Re are computed as:

$$Re = \frac{n\rho_f D_p}{\mu_f} \|\mathbf{U}_s - \mathbf{U}_f\| \quad (26)$$

293 The function $F(\phi_s, Re)$ can be calculated as:

$$F(\phi_s, Re) = F(\phi_s, 0) + \frac{0.413Re}{24(1-\phi_s)^2} \left(\frac{(1-\phi_s)^{-1} + 3\phi_s(1-\phi_s) + 8.4Re^{-0.343}}{1 + 10^{3\phi_s} Re^{-(1+4\phi_s)/2}} \right) \quad (27)$$

294 where the low Reynold coefficient $F(\phi_s, Re \rightarrow 0)$ is:

$$F(\phi_s, 0) = \frac{10\phi_s}{(1-\phi_s)^2} + (1-\phi_s)^2(1 + 1.5\sqrt{\phi_s}) \quad (28)$$

295 When validating the model with analytical solution, it requires to know the
 296 hydraulic conductivity K . In such case, we convert the equation (25) to
 297 Kozeny-Carman formula by assuming $F(\phi_s, Re) = 10\phi_s/(1-\phi_s)^2$, leading to

$$\mathbf{f}_d = \frac{180\phi_s^2\mu_f}{D_p^2(1-\phi_s)} (\mathbf{U}_s - \mathbf{U}_f) \quad (29)$$

298 Then, the draging force following the Darcy law is given by:

$$\mathbf{f}_d = \frac{n^2\mu_f}{\kappa} (\mathbf{U}_s - \mathbf{U}_f) \quad (30)$$

299 where κ being intrinsic permeability of soil which can be written as:

$$\kappa = \frac{K\mu_f}{\rho_f g} \quad (31)$$

300 As such, the hydraulic conductivity will be expressed as:

$$K = \frac{D_p^2(1-\phi_s)^3}{180\phi_s^2\mu_f} \rho_f g \quad (32)$$

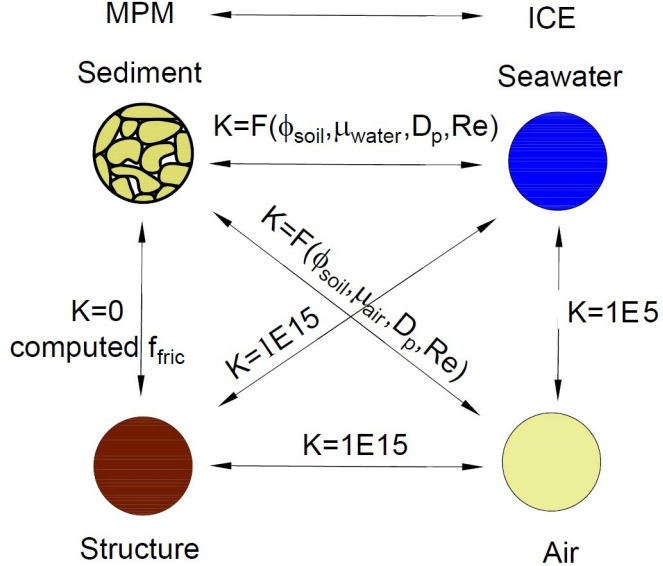


Figure 3: Momentum exchange coefficient between materials

301 Solving momentum and energy exchange with an implicit solver

302 The derivation of the implicit integration for the momentum exchange is
 303 presented in the Appendix's section 'Momentum and energy exchange with
 304 an implicit solver'. The linear equations for multi phases $i,j=1:N$ has the
 305 form as:

$$\begin{vmatrix} (1 + \beta_{ij}) & -\beta_{ij} \\ -\beta_{ji} & (1 + \beta_{ji}) \end{vmatrix} \begin{vmatrix} \Delta \mathbf{U}_i \\ \Delta \mathbf{U}_j \end{vmatrix} = \begin{vmatrix} \beta_{ij} (\mathbf{U}_i^* - \mathbf{U}_j^*) \\ \beta_{ji} (\mathbf{U}_i^* - \mathbf{U}_j^*) \end{vmatrix}$$

306 where the intermediate velocity for fluid phases $f=1:N_f$ and for solid/porous
 307 phases $s=1:N_s$ can be calculated by:

$$\begin{aligned} \mathbf{U}_f^* &= \mathbf{U}_f^n + \Delta t \left(-\frac{\nabla P_f^{n+1}}{\rho_f^n} + \frac{\nabla \cdot \boldsymbol{\tau}_f^n}{\bar{\rho}_f^n} + \mathbf{b} \right) \\ \mathbf{U}_s^* &= \mathbf{U}_s^n + \Delta t \left(\frac{\nabla \cdot \boldsymbol{\sigma}'^n}{\bar{\rho}_s^n} - \frac{\nabla P_f^{n+1}}{\rho_s} + \mathbf{b} \right) \end{aligned} \quad (33)$$

308 Also, the momentum exchange coefficient can be computed at every time
 309 step as $\beta_{12} = K/\bar{\rho}_f^n$ and $\beta_{21} = K/\bar{\rho}_s^n$ with the coefficient depending on the
 310 different type of interactions (see Figure 3) as for example:

311

- 312 1. The drag force is set to zero in soil-structure interactions, and instead
 313 the frictional force is computed.
 314 2. As a result of fluid-structure interaction, the momentum exchange coef-
 315 ficient should be extremely high (1E15) when the solid material points
 316 are considered to be zero-porosity/zero-permeability.
 317 3. In the case of soil-fluid interaction, the drag force is calculated using
 318 the equation (25). Considering that air has a much lower viscosity than
 319 water, its drag force is much lower than the drag force of water in a
 320 pore.
 321 4. A momentum exchange coefficient of 1E5 is applied between multiphase
 322 flows. This value is far higher than reality [29], but it is necessary to
 323 have enough numerical stability to conduct simulations in the numerical
 324 example.

325 Similar approach applied for the energy exchange term leading to:

$$\begin{vmatrix} (1 + \eta_{ij}) & -\eta_{ij} \\ -\eta_{ji} & (1 + \eta_{ji}) \end{vmatrix} \begin{vmatrix} \Delta T_i \\ \Delta T_j \end{vmatrix} = \begin{vmatrix} \eta_{ij}(T_i^n - T_j^n) \\ \eta_{ji}(T_j^n - T_i^n) \end{vmatrix}$$

326 with η being the energy exchange coefficient.

327 *Equation of state for fluid phases*

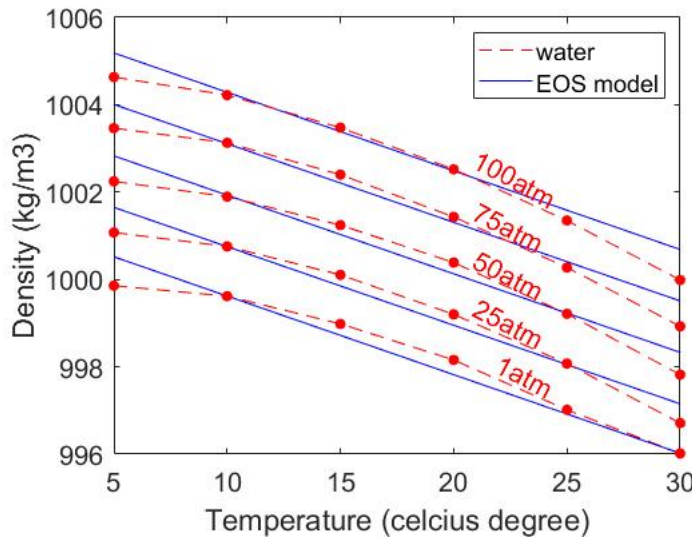


Figure 4: Equation of state of water

328 The equation of state establishes relations between thermodynamics vari-
 329 ables $[P_f, \rho_f, T_f]$. The choice of the equation of state depends on the types
 330 of the fluid materials. For example, for the air, it is possible to assume the
 331 equation of state for the perfect gas which obeys:

$$P_f = \rho_f R T_f \quad (34)$$

332 where R is the gas constant. For the water, a simple linear equation of state
 333 is in the following form:

$$P_f = P_{ref} + K_f(\rho_f - \rho_{ref} + \alpha_f(T_f - T_{ref})) \quad (35)$$

334 where reference pressure $P_{ref} = 1 \text{ atm} = 101325 \text{ Pa}$, reference temperature
 335 $T_{ref} = 10^\circ\text{C}$, reference density $\rho_{ref} = 999.8 \text{ kg/m}^3$, the bulk modulus of water
 336 $K_f = 2 \text{ GPa}$, and the water thermal expansion $\alpha_f = 0.18 \text{ }^\circ\text{C}^{-1}$. Equation
 337 (35) matches well with the state of the water (see Figure 4).

338 **Numerical implementation**

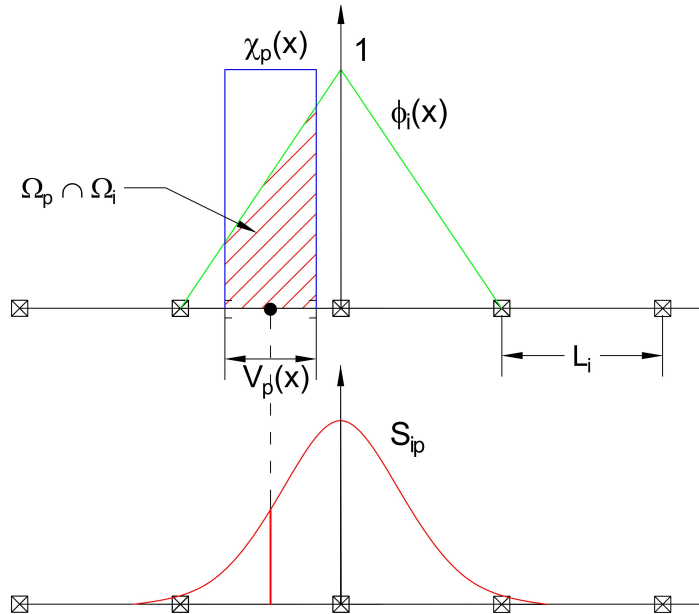


Figure 5: GIMP weighting function (red as a convolution of the linear basis shape function (green) and the characteristic function (blue))

339 The fluid phases are discretized in the grid with the state variables stored
 340 at the centroid of the cells $[\rho_{f,c}, \mathbf{U}_{f,c}, T_{f,c}, v_{f,c}]$ while the solid phase is dis-
 341 cretized in the particles with the state variables $[m_{sp}, \mathbf{U}_{sp}, T_{sp}, \boldsymbol{\sigma}'_{sp}]$. In the
 342 Material Point Method, we use the generalized interpolation technique [30]
 343 using the weight function as a convolution of a grid shape function $N_i(\mathbf{x})$ in
 344 a nodal domain Ω_i and a characteristic function $\chi_p(\mathbf{x})$ in a particle domain
 345 Ω_p with the volume $V_p(\mathbf{x})$ as follows:

$$S_{ip} = \frac{1}{V_p} \int_{\Omega_i \cap \Omega_p} N_i(\mathbf{x}) \chi_p(\mathbf{x}) d\mathbf{x} \quad (36)$$

346 where the volume $V_p(\mathbf{x})$ of the material point p can be calculated as:

$$V_p = \int_{\Omega_p} \chi_p(\mathbf{x}) d\mathbf{x} \quad (37)$$

347 The characteristic function is the Heaviside function as $\chi_p = 1$ if $\mathbf{x} \in \Omega_p$,
 348 otherwise 0 (see Figure 5). For the interpolation of the centroid of the cell,
 349 the linear basis function is used as:

$$S_{ci} = N_i(\mathbf{x}_c) \quad (38)$$

350 The time discretization are solved using the following steps.

351 *Interpolation from Solid Particle to Grid*

352 The nodal values of the solid state (mass, velocity, temperature, volume)
 353 are:

$$\begin{aligned} m_{si}^n &= \sum S_{ip} m_{sp} \\ \mathbf{U}_{si}^n &= \frac{\sum S_{ip} (m\mathbf{U})_{sp}^n}{m_{si}^n} \\ T_{si}^n &= \frac{\sum S_{ip} (mT)_{sp}^n}{m_{si}^n} \\ V_{si}^n &= \frac{\sum S_{ip} (mV)_{sp}^n}{m_{si}^n} \\ \boldsymbol{\sigma}_{si}^n &= \frac{\sum S_{ip} (\boldsymbol{\sigma}V)_{sp}^n}{V_{si}^n} \end{aligned} \quad (39)$$

354 The nodal internal forces is calculated by:

$$\mathbf{f}_{si}^{int,n} = - \sum \nabla S_{ip} (\boldsymbol{\sigma}'_{sp})^n V_{sp}^n \quad (40)$$

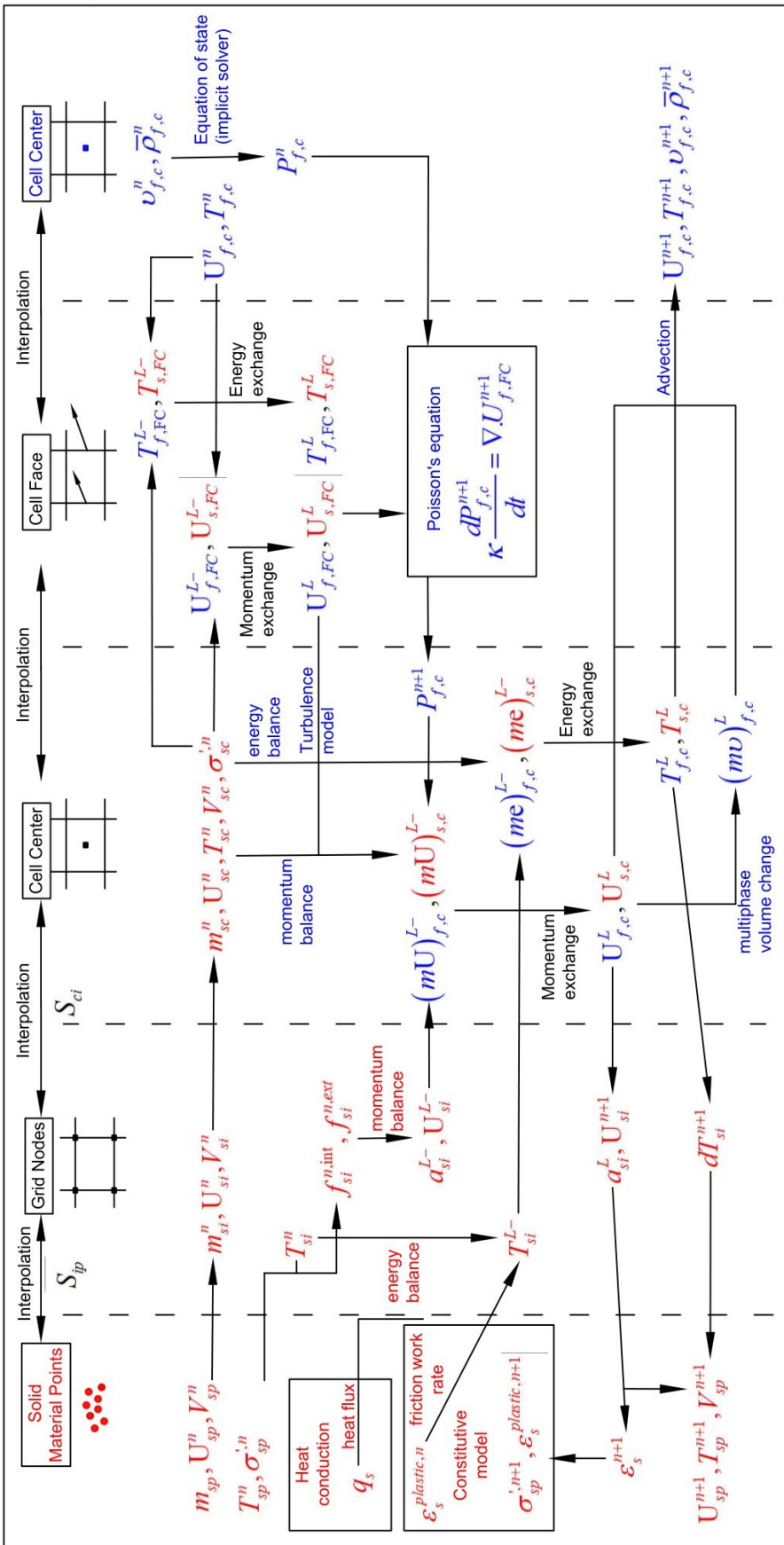


Figure 6: Numerical implementation of MPMICE

355 The nodal external forces $f_{si}^{ext,n}$ and the frictional forces from soil-structure
 356 interaction $f_{fric,si}^n$ from contact between materials are computed here.
 357 Then we compute the solid cell variables as:

$$\begin{aligned} m_{sc}^n &= \sum S_{ci} m_{si} \\ \rho_{sc}^n &= \frac{m_{sc}^n}{V} \\ \mathbf{U}_{sc}^n &= \sum S_{ci} \mathbf{U}_{si}^n \\ T_{sc}^n &= \sum S_{ci} T_{si}^n \\ V_{sc}^n &= \sum S_{ci} V_{si}^n \\ \boldsymbol{\sigma}_{sc}^n &= \sum S_{ci} \boldsymbol{\sigma}_{si}^n \end{aligned} \tag{41}$$

358 *Compute equation of state for fluid phase*

359 The total fluid material volume of a cell is:

$$V_{total} = \sum_{f=1}^{N_f} M_f v_f \tag{42}$$

360 We need to find $P_{f,c}^n$ which allows each fluid materials obey their equation of
 361 states $[P_f, \rho_f, v_f, T_f, e_f]$ but also allow mass of all fluid materials to fill the
 362 entire the pore volume without ongoing compression or expansion following
 363 the condition as follows:

$$0 = n - \sum_{f=1}^{N_f} v_f \bar{\rho}_f \tag{43}$$

364 Then, we can use the Newton-Raphson interation to find the value of $P_{f,c}^n$
 365 which satisfies the equation (42, 43) and each equation of states of each fluid
 366 materials.

367 *Compute cell face velocity*

368 Following the derivation in the Appendix: Advanced Fluid Pressure, we
 369 first compute the fluid cell face velocity as:

$$\mathbf{U}_{f,FC}^{L-} = \frac{(\bar{\rho} \mathbf{U})_{f,FC}^n}{\bar{\rho}_{f,FC}^n} + \Delta t \left(-\frac{\nabla^{FC} P_{f,c}^n}{\rho_{f,FC}^n} + \frac{\nabla^{FC} \cdot \boldsymbol{\tau}^n}{\bar{\rho}_{s,FC}} + \mathbf{b} \right) \tag{44}$$

³⁷⁰ The equation (44) is discretized in three dimension (noted that $\nabla^{FC} \cdot \boldsymbol{\tau} = 0$),
³⁷¹ for example the discretized equation in the x direction is:

$$U_{fx}^{L-} = \frac{(\bar{\rho}U)_{fx,R}^n + (\bar{\rho}U)_{fx,L}^n}{\bar{\rho}_{fx,L}^n + \bar{\rho}_{fx,R}^n} + \Delta t \left(-\frac{2(v_{fx,L}^n v_{fx,R}^n)}{v_{fx,L}^n + v_{fx,R}^n} \frac{P_{f,cx,R}^n - P_{f,cx,L}^n}{\Delta x} + b_x \right) \quad (45)$$

³⁷² The cell face solid velocity can be calculated as:

$$\mathbf{U}_{s,FC}^{L-} = \frac{(\bar{\rho}\mathbf{U})_{s,FC}^n}{\bar{\rho}_{s,FC}^n} + \Delta t \left(\frac{\nabla^{FC} \cdot \boldsymbol{\sigma}_c'^n}{\bar{\rho}_{s,FC}} - \frac{\nabla^{FC} P_{f,c}^n}{\rho_s} + \mathbf{b} \right) \quad (46)$$

³⁷³ The equation (46) is discretized in three dimension (noted that $\nabla^{FC} \cdot \boldsymbol{\sigma}_{ij} = 0$
³⁷⁴ with $i \neq j$), for example the discretized equation in the x direction is:

$$U_{sx}^{L-} = \frac{(\bar{\rho}U)_{sx,R}^n + (\bar{\rho}U)_{sx,L}^n}{\bar{\rho}_{sx,L}^n + \bar{\rho}_{sx,R}^n} + \Delta t \left(\frac{2(\sigma_{xx,R} - \sigma_{xx,L})}{(\bar{\rho}_{sx,L}^n + \bar{\rho}_{sx,R}^n) \Delta x} - \frac{P_{f,cx,R}^n - P_{f,cx,L}^n}{\rho_s \Delta x} + b_x \right) \quad (47)$$

³⁷⁵ Then, we compute the modified cell face velocity \mathbf{U}_{FC}^L considering the mo-
³⁷⁶ mentum exchange (see the Appendix: Momentum exchange with an implicit
³⁷⁷ solve) as follows:

$$\begin{aligned} \mathbf{U}_{f,FC}^L &= \mathbf{U}_{f,FC}^{L-} + \Delta \mathbf{U}_{f,FC} \\ \mathbf{U}_{s,FC}^L &= \mathbf{U}_{s,FC}^{L-} + \Delta \mathbf{U}_{s,FC} \end{aligned} \quad (48)$$

³⁷⁸ The linear equation below is solved to obtain the increment of velocity with
³⁷⁹ i,j = 1 : N as:

$$\begin{vmatrix} (1 + \beta_{ij}) & -\beta_{ij} \\ -\beta_{ji} & (1 + \beta_{ji}) \end{vmatrix} \begin{vmatrix} \Delta \mathbf{U}_{i,FC} \\ \Delta \mathbf{U}_{j,FC} \end{vmatrix} = \begin{vmatrix} \beta_{ij} (\mathbf{U}_{i,FC}^{L-} - \mathbf{U}_{j,FC}^{L-}) \\ \beta_{ji} (\mathbf{U}_{j,FC}^{L-} - \mathbf{U}_{i,FC}^{L-}) \end{vmatrix}$$

³⁸⁰ Compute cell face temperature

³⁸¹ Similar to the velocity, the faced temperature is computed, for example
³⁸² in x direction, as:

$$\begin{aligned} T_{fx}^{L-} &= \frac{(\bar{\rho}T)_{fx,R}^n + (\bar{\rho}T)_{fx,L}^n}{\bar{\rho}_{fx,L}^n + \bar{\rho}_{fx,R}^n} \\ T_{sx}^{L-} &= \frac{(\bar{\rho}T)_{sx,R}^n + (\bar{\rho}T)_{sx,L}^n}{\bar{\rho}_{sx,L}^n + \bar{\rho}_{sx,R}^n} \end{aligned} \quad (49)$$

³⁸³ Then, we compute the modified cell face temperature T_{FC}^L considering the
³⁸⁴ energy exchange (see the Appendix: Momentum and energy exchange with

385 an implicit solver) as follows:

$$\begin{aligned} T_{f,FC}^L &= T_{f,FC}^{L-} + \Delta T_{f,FC} \\ T_{s,FC}^L &= T_{s,FC}^{L-} + \Delta T_{s,FC} \end{aligned} \quad (50)$$

386 The linear equation below is solved to determine the increment of tempera-
387 ture due to energy exchange with $i,j = 1 : N$ as:

$$\begin{vmatrix} (1 + \eta_{ij}) & -\eta_{ij} \\ -\eta_{ji} & (1 + \eta_{ji}) \end{vmatrix} \begin{vmatrix} \Delta T_{i,FC} \\ \Delta T_{j,FC} \end{vmatrix} = \begin{vmatrix} \eta_{ij}(T_{i,FC}^{L-} - T_{j,FC}^{L-}) \\ \eta_{ji}(T_{j,FC}^{L-} - T_{i,FC}^{L-}) \end{vmatrix}$$

388 *Compute fluid pressure (implicit scheme)*

389 For single phase flow, the increment of the fluid pressure can be computed
390 as:

$$\kappa_f \frac{\Delta P}{dt} = \nabla^c \cdot \mathbf{U}_{f,FC}^{n+1} \quad (51)$$

391 For multi-phase flows, the increment of the fluid pressure of the mixture can
392 be computed as:

$$\kappa \frac{\Delta P}{dt} = \sum_{f=1}^{N_f} \nabla^c \cdot (\phi_{f,FC} \mathbf{U}_{f,FC})^{n+1} \quad (52)$$

393 where $\kappa = \sum_{f=1}^{N_f} (\phi_{f,FC} \kappa_f) / \sum_{f=1}^{N_f} (\phi_{f,FC})$. Then, the fluid pressure at cell
394 center is:

$$P_c^{n+1} = P_c^n + \Delta P_c^n \quad (53)$$

395 Finally, the cell face advanced fluid pressure is:

$$P_{FC}^{n+1} = \left(\frac{P_{c,L}^{n+1}}{\bar{\rho}_{f,L}^n} + \frac{P_{c,R}^{n+1}}{\bar{\rho}_{f,R}^n} \right) / \left(\frac{1}{\bar{\rho}_{f,L}^n} + \frac{1}{\bar{\rho}_{f,R}^n} \right) = \left(\frac{P_{c,L}^{n+1} \bar{\rho}_{f,R}^n + P_{c,R}^{n+1} \bar{\rho}_{f,L}^n}{\bar{\rho}_{f,L}^n \bar{\rho}_{f,R}^n} \right) \quad (54)$$

396 *Compute viscous shear stress term of the fluid phase*

397 This part compute the viscous shear stress $\Delta(m\mathbf{U})_{f,c,\tau}$ for a single vis-
398 cous compressible Newtonian fluid and optionally shear stress induced by the
399 turbulent model.

400 *Compute nodal internal temperature of the solid phase*

401 The nodal internal temperature rate is computed based on the heat con-
402 duction model as below:

$$dT_{si}^{L-} = \frac{(\Delta W_{si}^n + \Delta W_{fric,i}^n + \nabla^i \cdot \mathbf{q}_{si}^n)}{m_{si}^n c_v} \quad (55)$$

403 where $\Delta W_{si}^n = \boldsymbol{\sigma}' : \frac{D_s(\boldsymbol{\epsilon}_s^p)}{Dt}$ is the mechanical work rate computed from the
404 constitutive model with $\boldsymbol{\epsilon}_s^p$ is the plastic strain, $\Delta W_{fric,i}^n$ is the work rate
405 computed from the contact law due to the frictional sliding between solid
406 materials. The heat flux is $\mathbf{q}_s = \bar{\rho}_s \beta_s \nabla T_s$ with β_s being the thermal conduc-
407 tivity of the solid materials.

$$T_{si}^{L-} = T_{si}^n + dT_{si}^{L-} \quad (56)$$

408 *Compute and integrate acceleration of the solid phase*

409 After interpolating from material points to the nodes, the nodal acceler-
410 ation and velocity are calculated by:

$$\mathbf{a}_{si}^{L-} = \frac{\mathbf{f}_{si}^{int,n} + \mathbf{f}_{si}^{ext,n}}{m_{si}^n} + \mathbf{g} \quad (57)$$

$$\mathbf{U}_{si}^{L-} = \mathbf{U}_{si}^n + \mathbf{a}_{si}^{L-} \Delta t \quad (58)$$

412 *Compute Lagrangian value (mass, momentum and energy)*

413 For the fluid phase, the linear momentum rate, the energy rate are:

$$\Delta(m\mathbf{U})_{f,c} = V n_c^n \nabla^c P_c^{n+1} + \Delta(m\mathbf{U})_{f,c,\tau} + V \bar{\rho}_{f,c}^n g \quad (59)$$

$$\Delta(me)_{f,c} = V n_c^n P_c^{n+1} \nabla^c \cdot \mathbf{U}_{f,FC}^* + \nabla^c \cdot \mathbf{q}_{f,c}^n \quad (60)$$

415 The heat flux is $\mathbf{q}_f = \bar{\rho}_f \beta_f \nabla T_f$ with β_f being the thermal conductivity of the
416 fluid materials. The Lagrangian value of the mass, linear momentum and
417 energy of fluid phases without momentum exchange are:

$$m_{f,c}^L = V \bar{\rho}_{f,c}^n \quad (61)$$

$$(m\mathbf{U})_{f,c}^{L-} = V \bar{\rho}_{f,c}^n \mathbf{U}_{f,c}^n + \Delta(m\mathbf{U})_{f,c} \quad (62)$$

$$(me)_{f,c}^{L-} = V \bar{\rho}_{f,c}^n T_{f,c}^n c_v + \Delta(me)_{f,c} \quad (63)$$

⁴²⁰ For the solid phase, the Lagrangian value of the linear momentum and energy
⁴²¹ of solid phase are:

$$m_{sc}^L = m_{sc}^n \quad (64)$$

$$(m\mathbf{U})_{sc}^{L-} = \sum S_{ci} m_{si}^n \mathbf{U}_{si}^{L-} + V(1 - n_c^n) \nabla^c P_{f,c}^{n+1} \quad (65)$$

$$(me)_{sc}^{L-} = \sum S_{ci} m_{si}^n T_{si}^L c_v \quad (66)$$

⁴²⁴ To consider the momentum exchange, the Lagrangian velocity is modified as:

$$\begin{aligned} \mathbf{U}_{f,c}^L &= \mathbf{U}_{f,c}^{L-} + \Delta \mathbf{U}_{f,c} \\ \mathbf{U}_{sc}^L &= \mathbf{U}_{sc}^{L-} + \Delta \mathbf{U}_{sc} \end{aligned} \quad (67)$$

⁴²⁵ where the cell-centered intermediate velocity can be calculated by:

$$\begin{aligned} \mathbf{U}_{f,c}^{L-} &= \frac{(m\mathbf{U})_{f,c}^{L-}}{m_{f,c}^L} \\ \mathbf{U}_{sc}^{L-} &= \frac{(m\mathbf{U})_{sc}^{L-}}{m_{sc}^L} \end{aligned} \quad (68)$$

⁴²⁶ And the increment of the velocity $\mathbf{U}_{f,c}$, $\Delta \mathbf{U}_{sc}$ can be computed by solving
⁴²⁷ the linear equation with $i,j = 1:N$ as:

$$\begin{vmatrix} (1 + \beta_{ij}) & -\beta_{ij} \\ -\beta_{ji} & (1 + \beta_{ji}) \end{vmatrix} \begin{vmatrix} \Delta \mathbf{U}_{i,c} \\ \Delta \mathbf{U}_{j,c} \end{vmatrix} = \begin{vmatrix} \beta_{ij} (\mathbf{U}_{i,c}^{L-} - \mathbf{U}_{j,c}^{L-}) \\ \beta_{ji} (\mathbf{U}_{j,c}^{L-} - \mathbf{U}_{i,c}^{L-}) \end{vmatrix}$$

⁴²⁸ To consider the energy exchange, the Lagrangian temperature is modified as:

$$\begin{aligned} T_{f,c}^L &= T_{f,c}^{L-} + \Delta T_{f,c} \\ T_{sc}^L &= T_{sc}^{L-} + \Delta T_{sc} \end{aligned} \quad (69)$$

⁴²⁹ where the cell-centered intermediate temperature can be calculated by:

$$\begin{aligned} T_{f,c}^{L-} &= \frac{(mT)_{f,c}^{L-}}{m_{f,c}^L c_v} \\ T_{sc}^{L-} &= \frac{(mT)_{sc}^{L-}}{m_{sc}^L c_v} \end{aligned} \quad (70)$$

⁴³⁰ And the increment of the temperature due to energy exchange can be com-
⁴³¹ puted by solving the linear equation with $i,j = 1:N$ as:

$$\begin{vmatrix} (1 + \eta_{ij}) & -\eta_{ij} \\ -\eta_{ji} & (1 + \eta_{ji}) \end{vmatrix} \begin{vmatrix} \Delta T_{i,c} \\ \Delta T_{j,c} \end{vmatrix} = \begin{vmatrix} \eta_{ij} (T_{i,c}^{L-} - T_{j,c}^{L-}) \\ \eta_{ji} (T_{j,c}^{L-} - T_{i,c}^{L-}) \end{vmatrix}$$

⁴³² Finally, we obtain the cell-centered solid acceleration and temperature rate
⁴³³ as:

$$d\mathbf{U}_{sc}^L = \frac{(m\mathbf{U})_{sc}^L - (m\mathbf{U})_{sc}^n}{m_{sc}^L \Delta t} \quad (71)$$

$$dT_{sc}^L = \frac{(me)_{sc}^L - (me)_{sc}^n}{m_{sc}^L c_v \Delta t} \quad (72)$$

⁴³⁵ *Compute Lagrangian specific volume of the fluid phase*

⁴³⁶ To compute the Lagrangian value of the specific volume of the fluid phase,
⁴³⁷ we need to compute the Lagrangian temperature rate as below:

$$T_{f,c}^{n+1} = \frac{(me)_{f,c}^L}{m_{f,c}^L c_v} \quad (73)$$

$$\frac{D_f T_{f,c}}{Dt} = \frac{T_{f,c}^{n+1} - T_{f,c}^n}{\Delta t} \quad (74)$$

⁴³⁹ As such, the Lagrangian specific volume rate is:

$$\Delta(mv)_{f,c} = V f_{f,c}^\phi \nabla \cdot \mathbf{U} + (\phi_{f,c} \alpha_{f,c} \frac{D_f T_{f,c}}{Dt} - f_{f,c}^\phi \sum_{n=1}^N \phi_{nc} \alpha_{nc} \frac{D_n T_{n,c}}{Dt}) \quad (75)$$

⁴⁴⁰ where $f_f^\phi = (\phi_f \kappa_f) / (\sum_{n=1}^N \phi_n \kappa_n)$ and $\mathbf{U} = \nabla \cdot (\sum_{s=1}^{N_s} \phi_{sc} \mathbf{U}_{sc} + \sum_{f=1}^{N_f} \phi_{fc} \mathbf{U}_{f,c})$.
⁴⁴¹ Finally, the Lagrangian specific volume is:

$$(mv)_{f,c}^L = V \bar{\rho}_{f,c}^n v_{f,c}^n + \Delta(mv)_{f,c} \quad (76)$$

⁴⁴² *Compute advection term and advance in time*

⁴⁴³ The mass, linear momentum, energy and specific volume with advection
⁴⁴⁴ are:

$$m_{f,c}^{n+1} = m_{f,c}^L - \Delta t \nabla \cdot (\bar{\rho}_{f,c}^L, \mathbf{U}_{f,FC}^L) \quad (77)$$

$$(m\mathbf{U})_{f,c}^{n+1} = (m\mathbf{U})_{f,c}^L - \Delta t \nabla \cdot ((\bar{\rho}\mathbf{U})_{f,c}^L, \mathbf{U}_{f,FC}^L) \quad (78)$$

$$(me)_{f,c}^{n+1} = (me)_{f,c}^L - \Delta t \nabla \cdot ((\bar{\rho}c_v T)_{f,c}^L, \mathbf{U}_{f,FC}^L) \quad (79)$$

$$(mv)_{f,c}^{n+1} = (mv)_{f,c}^L - \Delta t \nabla \cdot ((\bar{\rho}v)_{f,c}^L, \mathbf{U}_{f,FC}^L) \quad (80)$$

⁴⁴⁸ Finally, the state variables of the fluid phases of the next time step are:

$$\bar{\rho}_{f,c}^{n+1} = \frac{m_{f,c}^{n+1}}{V} \quad (81)$$

449

$$\mathbf{U}_{f,c}^{n+1} = \frac{(m\mathbf{U})_{f,c}^{n+1}}{m_{f,c}^{n+1}} \quad (82)$$

450

$$T_{f,c}^{n+1} = \frac{(me)_{f,c}^{n+1}}{m_{f,c}^{n+1}} \quad (83)$$

451

$$v_{f,c}^{n+1} = \frac{(mv)_{f,c}^{n+1}}{m_{f,c}^{n+1}} \quad (84)$$

452 *Interpolate from cell to node of the solid phase*

453 First we interpolate the acceleration, velocity and temperature rate to
454 the node as below:

455

$$\mathbf{a}_{si}^n = \sum S_{ci} d\mathbf{U}_{sc}^L \quad (85)$$

456

$$\mathbf{U}_{si}^{n+1} = \sum S_{ci} d\mathbf{U}_{sc}^L \Delta t \quad (86)$$

457

$$dT_{si}^n = \sum S_{ci} dT_{sc}^L \quad (87)$$

458 Then the boundary condition and contact forces f_{si}^{fric} are applied to the nodal
velocity, and then accelerations are modified by:

$$\mathbf{a}_{si}^n = \frac{\mathbf{v}_{si}^{n+1} - \mathbf{v}_{si}^n}{\Delta t} \quad (88)$$

459 *Update the particle variables*

460 The state variables of the solid phase $[\mathbf{U}_{sp}^{n+1}, \mathbf{x}_{sp}^{n+1}, \nabla \mathbf{U}_{sp}^{n+1}, T_{sp}^{n+1}, \nabla T_{sp}^{n+1}, \mathbf{F}_{sp}^{n+1}, V_{sp}^{n+1}]$
461 (velocity, position, velocity gradient, temperature, temperature gradient, de-
462 formation gradient, volume) are updated as:

463

$$\mathbf{U}_{sp}^{n+1} = \mathbf{U}_{sp}^n + \sum S_{sp} \mathbf{a}_{si}^n \Delta t \quad (89)$$

464

$$\mathbf{x}_{sp}^{n+1} = \mathbf{x}_{sp}^n + \sum S_{sp} \mathbf{U}_{si}^{n+1} \Delta t \quad (90)$$

465

$$\nabla \mathbf{U}_{sp}^{n+1} = \sum \nabla S_{sp} \mathbf{U}_{si}^{n+1} \quad (91)$$

466

$$T_{sp}^{n+1} = T_{sp}^n + \sum S_{sp} dT_{si}^n \Delta t \quad (92)$$

467

$$\nabla T_{sp}^{n+1} = \sum \nabla S_{sp} T_{sp}^n \Delta t \quad (93)$$

467 $\mathbf{F}_{sp}^{n+1} = (\mathbf{I} + \nabla \mathbf{U}_{sp}^{n+1} \Delta t) \mathbf{F}_{sp}^n$ (94)

468 $V_{sp}^{n+1} = \det(\mathbf{F}_{sp}^{n+1}) V_{sp}^o$ (95)

469 Finally, the effective stress $(\sigma')^{n+1}$ is updated from the constitutive model
470 and the pore water pressure is interpolated from the cell as:

$$p_f^{n+1} = \sum S_{si} P_c^{n+1} \quad (96)$$

471 **Numerical validation**

472 All input files and the analytical calculations in this section are provided
473 in the Github repository (https://github.com/QuocAnh90/Uintah_NTNU)
474 for the reproduction of the numerical results.

475 For all simulations, the water has a bulk modulus of 2 GPa, a density of
476 998 kg/m³ at a reference temperature of 5 degrees Celsius and a reference
477 pressure of 10325 Pa (1atm), a dynamic viscosity μ_f of 1 mPa s). The air
478 has a ideal gas with a density of 1.17 kg/m³ at a reference temperature of
479 5 degrees Celsius and a reference pressure of 10325 Pa (1atm), a dynamic
480 viscosity μ_f of $18.45E^{-3}$ mPa s).

481 *Fluid Flow through isothermal porous media*

482 Fluid flow through porous media is important in many engineering disci-
483 plines, like predicting water flow in soil. Fluid flow velocity in one dimension
484 can be calculated from the porous media's hydraulic conductivity K as:

485 $U_f = K \frac{\Delta p_f}{L}$ (97)

486 If the Carman-Kozeny formula is adopted $F = 10\phi_s/(1 - \phi_s)^2$, the hydraulic
487 conductivity will be expressed as $K = D_p^2(1 - \phi_s)^3 \rho_f g / 180\phi_s^2 \mu_f$. Then, the
488 analytical formula of average velocity in one dimension through the porous
489 media is:

490 $U_f = \frac{1}{n} \frac{D_p^2(1 - \phi_s)^3}{180\phi_s^2 \mu_f} \frac{\Delta p_f}{L}$ (98)

491 Our numerical model is validated by modeling fluid flow through a 1m
492 long porous media. The porous media is modeled by elastic material with
493 Young's modulus is 10 MPa, Poisson's ratio is 0.3, and density is 2650 kg/m³.

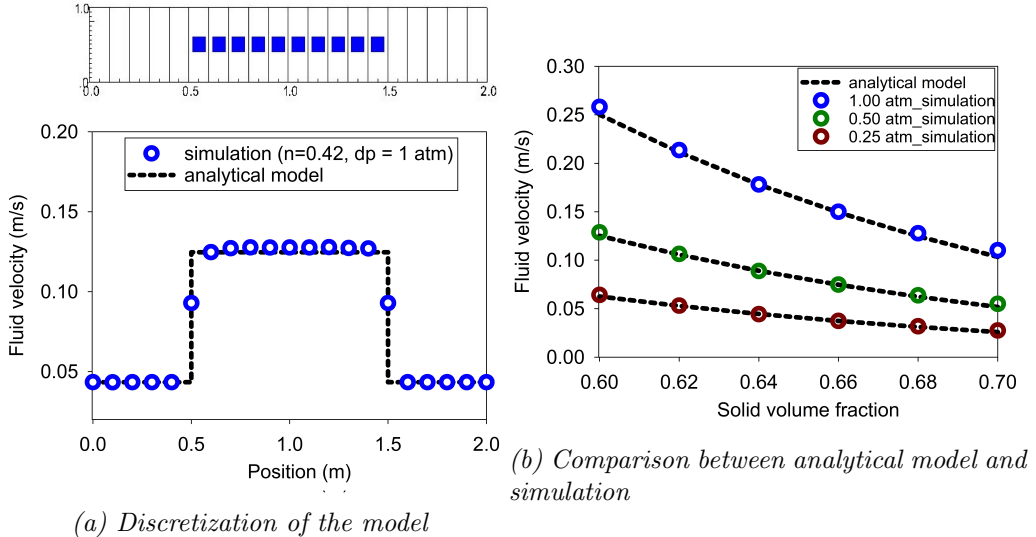


Figure 7: Numerical results of the fluid flow through isothermal porous media

The volume fraction of porous media ϕ_s is [0.6, 0.62, 0.66, 0.68, 0.7] and the average grain diameter d is 1mm. The model is discretized in 20 finite element and the porous media in 10 finite element with 1 material point per element. The pressure gradient is applied with three different value [0.25, 0.5, 1] atm. Figure 7 shows a good agreement of fluid flow prediction between the theory and the model.

500 Isothermal consolidation

A common benchmark for a fully saturated porous media is the simulation of one-dimensional consolidation. Using the Carman-Kozeny formula, the time-dependent pressure can be calculated as:

$$p_f = \sum_{m=1}^{\infty} \frac{2F_{ext}}{M} \sin\left(\frac{Mz}{H}\right) e^{-M^2 T_v} \text{ with } M = \frac{\pi}{2}(2m+1) \quad (99)$$

where the consolidation rate $T_v = C_v t / H^2$, the consolidation coefficient $C_v = E_v n^3 d^2 / (180(1-n)^2 \mu)$ and the Oedometer modulus $E_v = E(1-v)/(1+v)/(1-2v)$. Our numerical model is validated by modeling the consolidation of a 1m column. The porous media is modeled by elastic material with Young's modulus is 10 MPa, Poisson's ratio is 0.3, and density is 2650 kg/m3. The volume fraction of porous media ϕ_s is 0.7 which is equivalent to the

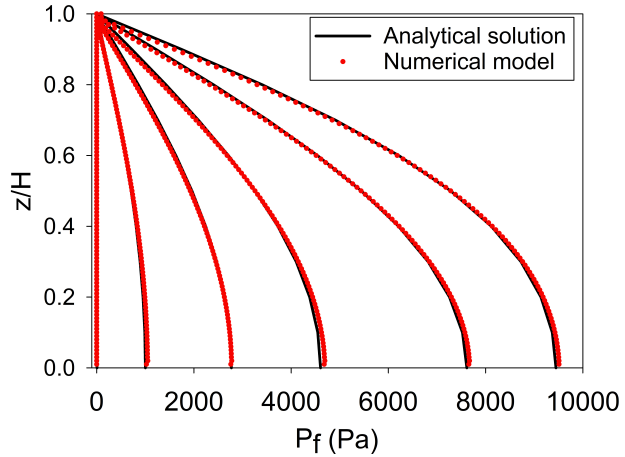


Figure 8: Comparison between analytical solution and numerical solution

porosity of 0.3 and the average grain diameter d is 1mm. The model is discretized in 100 finite element with 1 material point per element. The external pressure applies to the top of the column is 10 kPa. Figure 8 shows a good agreement of fluid flow prediction between the theory and the model.

514 *Thermal induced cavity flow*

Another benchmark is the thermal induced cavity flow in porous media. Temperature and velocity distributions are calculated for a square non-deformable saturated porous media. The top and bottom walls are insulated, and the left and right walls are at fixed temperature gradient of 1 degree. The fluid motion at steady state are cavity flow due to the temperature induced density variation. The numerical is validated by comparing with the numerical solution of the finite element method. The porous media is modeled by non deformable material, and density is 2500 kg/m³. The specific heat capacity of the water and porous skeleton are 4181 J/kg.K and 835 J/kg.K respectively. The thermal conductivity of the water and porous skeleton are 0.598 W/m.K and 0.4 W/m.K. The volume fraction of porous media ϕ_s is 0.6 which is equivalent to the porosity of 0.4 and the average grain diameter d is 1mm. The model is discretized in 20 x 20 finite element with 4 material point per element. Figure 10 shows a good agreement of numerical results of the model compared with the numerical solution of the finite element method.

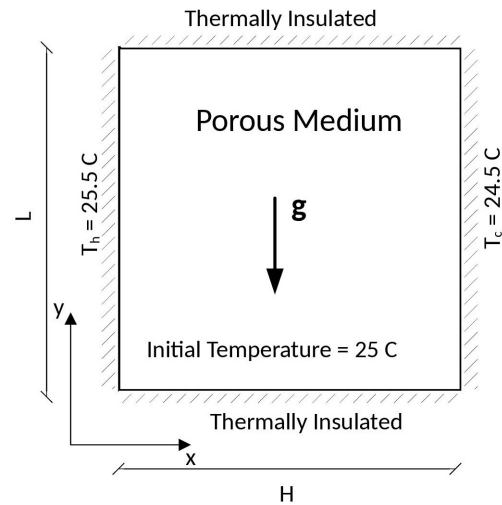


Figure 9: Model schematic [31]

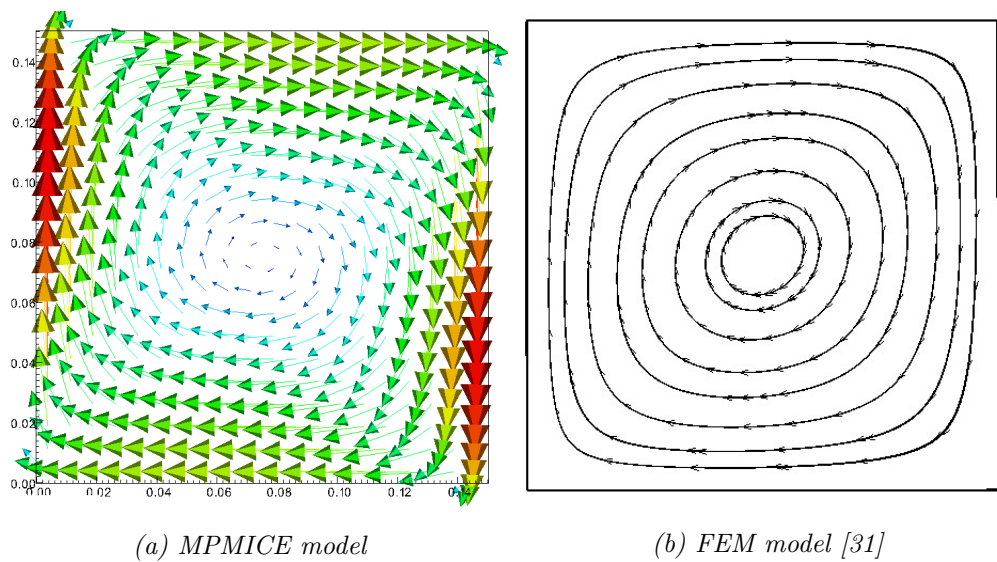


Figure 10: Comparison between MPMICE model and FEM model

530 **Numerical examples**

531 *Underwater debris flow*

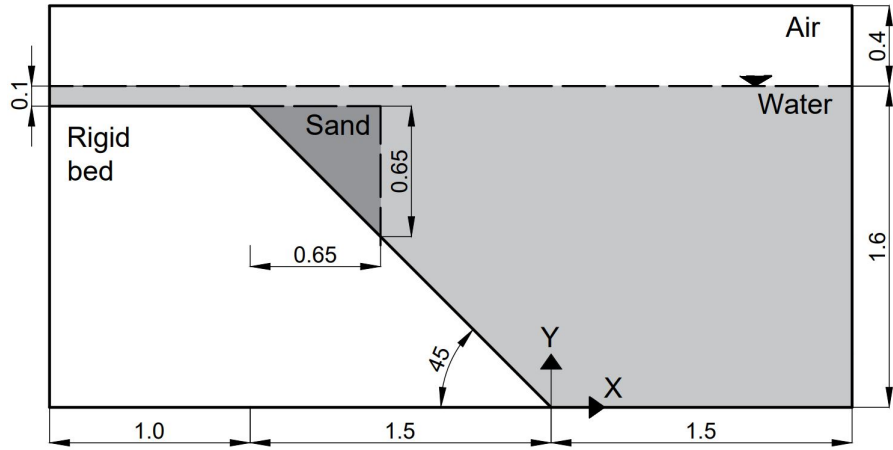


Figure 11: Model schematic

532 The numerical example is compared using the experimental work of Rzad-
 533 kiewicz et al. on submarine debris flow [32]. In their experiment, sand within
 534 a triangular box is released and slides along a rigid bed inclined at 45 degrees
 535 under water (see Figure 11). The material properties in the numerical model
 536 are selected based on the experiment by Rzadkiewicz et al. [32]. The sand
 537 is characterized by a saturated density of 1985 kg/m^3 and a friction angle
 538 of 10 degrees. The effect of Young's modulus on debris flow run-out is neg-
 539 ligible due to the extreme deformation of the debris, so a Young's modulus
 540 of 50 MPa with a Poisson's ratio of 0.25 is chosen. The rigid bed, being
 541 much stiffer, has bulk modulus and shear modulus values of $117E^7 \text{ Pa}$ and
 542 $43.8E^7 \text{ Pa}$, respectively. The numerical parameters used in this example are
 543 presented in Table 1.

544 The boundary conditions imposed in the numerical model are as follows: on
 545 all boundary faces, the velocity is set to zero ($U = 0 \text{ m/s}$) and the tempera-
 546 ture is set to 5 degrees Celsius ($T = 5^\circ\text{C}$). At the top boundary, the pressure
 547 has a Neumann boundary condition of $d\bar{p}/dx = 0 \text{ kPa}$, and the density has
 548 a Neumann boundary condition of $d\rho/dx = 0 \text{ kg/m}^3$. The background mesh
 549 consists of 700×400 cells, resulting in a total of 280,000 cells. Each cell in
 550 the debris flow and rigid bed contains 2×2 material points.

551 Figure 12b illustrates snapshots of the underwater debris flow sliding, demon-
 552 strating that the model captures the typical hydroplaning mechanism of the
 553 debris flow. Hydroplaning refers to the lifting of the debris flow, causing it
 554 to lose contact with the bottom layer. The elevation of the free surface at
 555 0.4s and 0.8s is compared between our proposed method and other methods
 556 in Figure 13. Our computed results align well with the experimental results
 557 [7].

558 Unlike other computational models that rely on total stress analysis [5, 6, 7,
 559 8], our proposed model utilizes effective stress analysis, enabling the analy-
 560 sis of water pressure and temperature within the debris flow. Additionally,
 561 we investigate the differences between underwater debris flow and saturated
 562 debris flow in terms of their interaction with obstacles. Figure 12 presents
 563 snapshots of simulations of both underwater and saturated debris flow. The
 564 saturated debris flow (Figure 12a) exhibits behavior similar to frictional flow,
 565 where grains have contact forces with each other. Conversely, the underwa-
 566 ter debris flow (Figure 12b) behaves like turbulent flow, with grains being
 567 separated from each other and exhibiting no contact forces (as reflected by
 the near-zero effective stress in the turbulence domain).

Materials	Bulk modul (Pa)	Shear modul (Pa)	Density (kg/m3)	Temp (C)	Dynamic viscosity (Pa s)	Friction angle (degrees)
Water (at surface)	2.15e9	-	999.8	5	855e-6	-
Air (at top boundary)	-	-	1.177	5	18.45e-6	-
Sand (porous media)	8.33e6	20e6	1985	5	-	10
Rigid bed (solid)	117e7	43.8e7	8900	5	-	-

Table 1: Numerical parameters for the underwater submarine debris flow

568

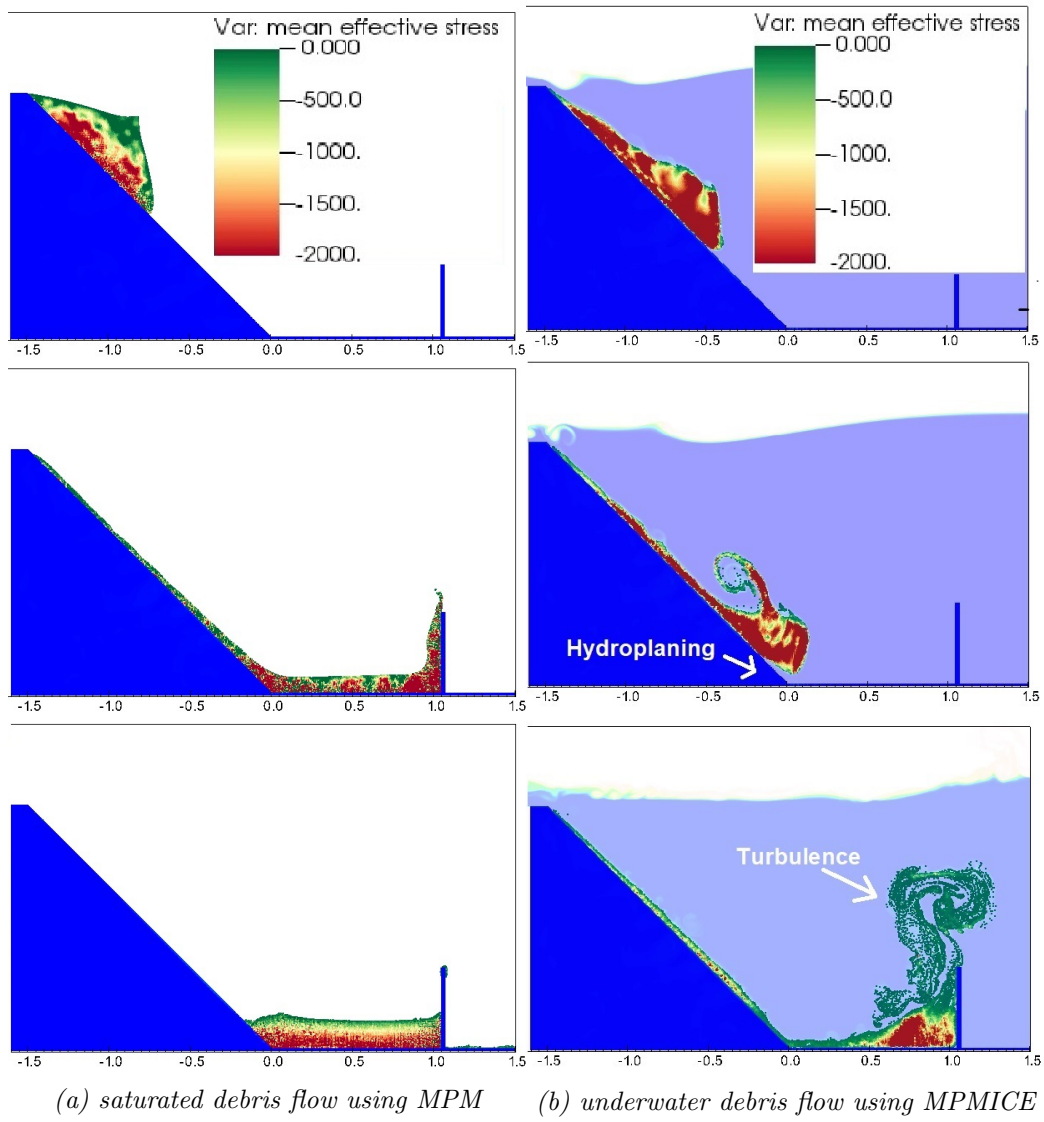
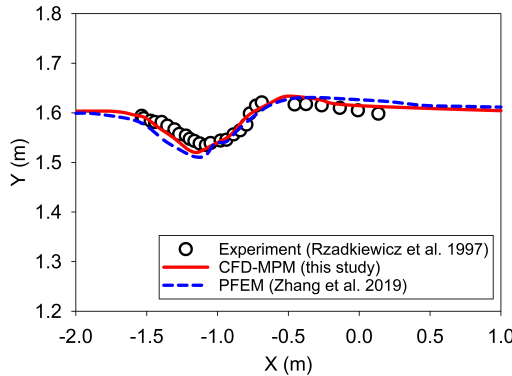
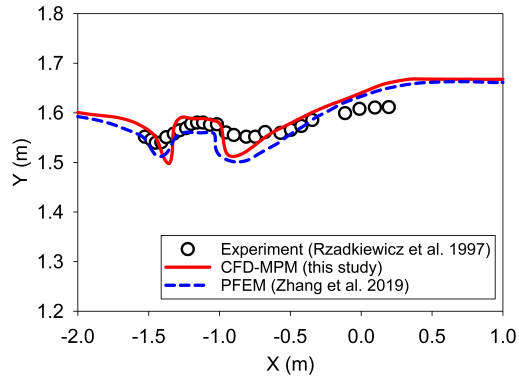


Figure 12: Simulation of Debris Flow: Mean Effective Stress Distribution (Green Color Indicates Near-Zero Effective Stress)



(a) 0.4 seconds



(b) 0.8 seconds

Figure 13: Evolution of water level in the simulation of underwater debris flow

569 Validation of soil response to the seismic loading

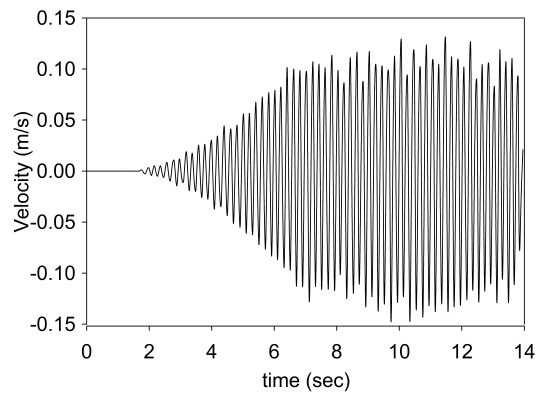


Figure 14: Seismic loading

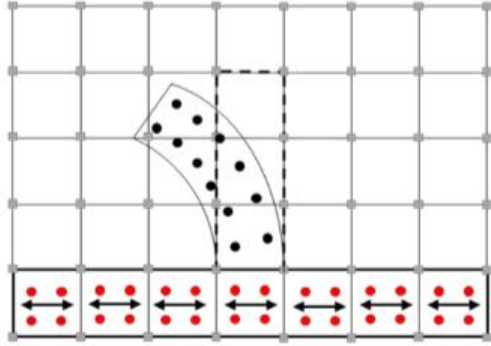


Figure 15: Material points prescribed velocity as kinematic boundary condition [33]

570 An experimental study conducted by Hiraoka et al. [34] aimed to invest-
 571 tigate the influence of seismic shaking on the deformation of a 0.5 m-high
 572 sand slope. The sand used in the experiment was partially saturated, with a
 573 moisture content of 10 percent. The provided soil parameters for the Mohr
 574 Coulomb model include the effective friction angle of 23 degrees, apparent
 575 cohesion of 0.78 kPa, Young's modulus of 2.57 MPa, and Poisson's ratio of
 576 0.33, and moist unit weight of 16.5 kN/m³. The soil's dilatancy angle was
 577 assumed to be 0 [34]. The experimental setup consisted of a shaking table
 578 box with a steel horizontal base and smooth glass vertical sidewalls. Laser
 579 sensors were used to monitor the displacement of the slope's toe and crest.
 580 Figure 14 displays the velocity-time history employed in the experiment.

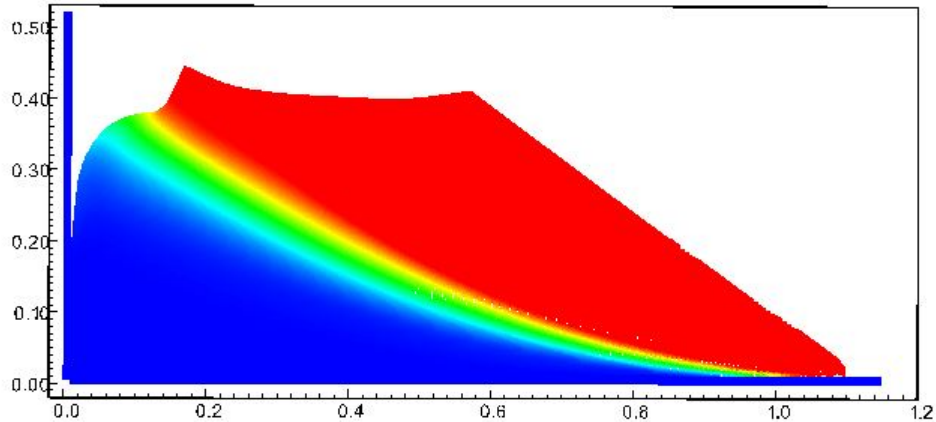


Figure 16: Numerical model of the seismic-induced slope failure with displacement color

581 To simulate the seismic loading in our numerical model, we adopted a
 582 method presented by Alsardi et al. [33], which involves specifying the velocity
 583 at the corresponding material points representing either the shaking table or
 584 the bedrock at the site (see Figure 15). In our simulation, we considered the
 585 horizontal base to be fully rough and the vertical contact to be fully smooth.
 586 The initial stress condition was initiated using gravity and seismic loading
 587 induced the slope failure (see Figure 16).

588 Previous studies by Bhandari et al. [35], Alsardi et al. [33], and Hiraoka et
 589 al. [34] attempted to model this experiment using MPM and SPH models. In
 590 this study, we compared our results with those obtained from other particle-
 591 based methods (Figure 17). The main difference is that we did not apply
 592 5 percent numerical damping in our model, unlike the other methods. We
 593 found that the final displacement of the slope toe in our MPM model was
 594 higher than that observed in the experiment. Nevertheless, the validation of
 595 the Mohr-Coulomb model under seismic response demonstrated a reasonable
 596 soil behavior in terms of displacement.

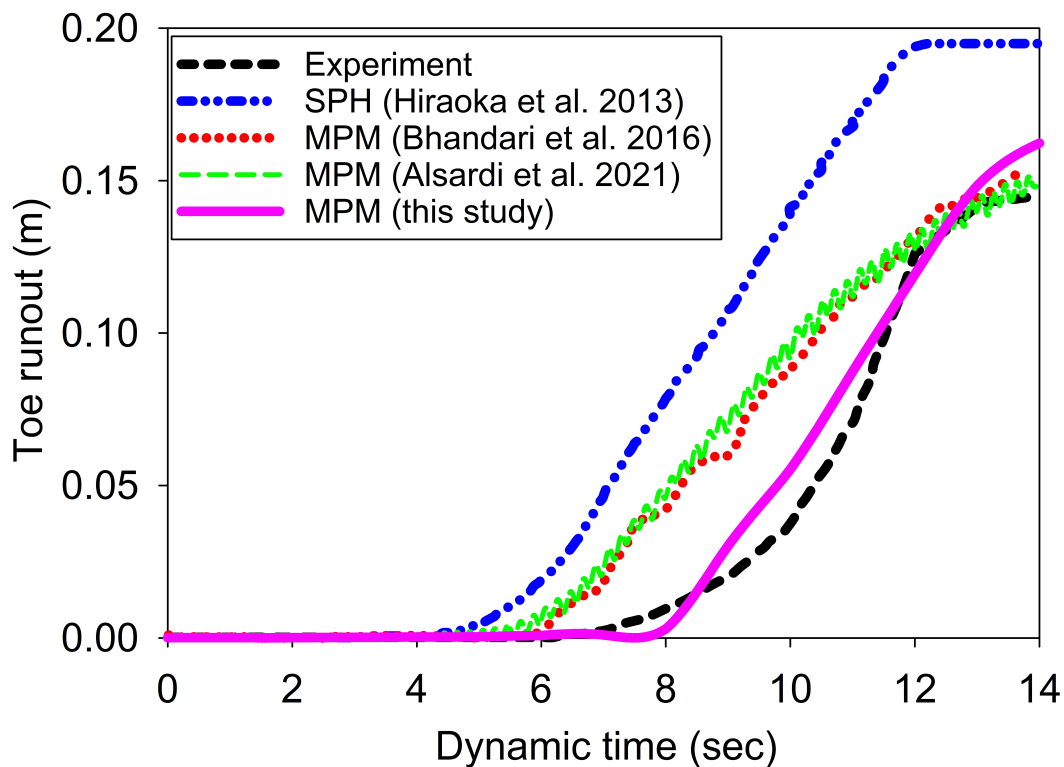


Figure 17: Displacement of the toe of the slope

597 Earthquake-induced submarine landslides

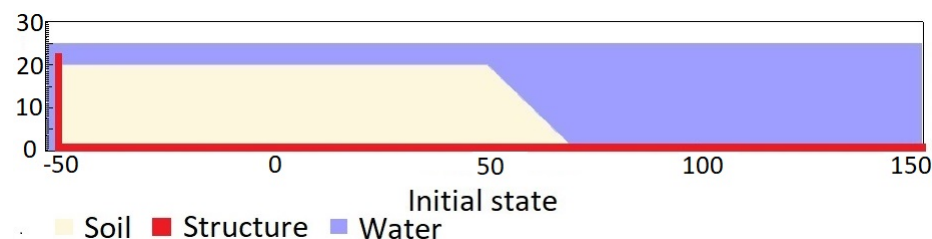


Figure 18: Numerical simulation of the earthquake-induced submarine landslide

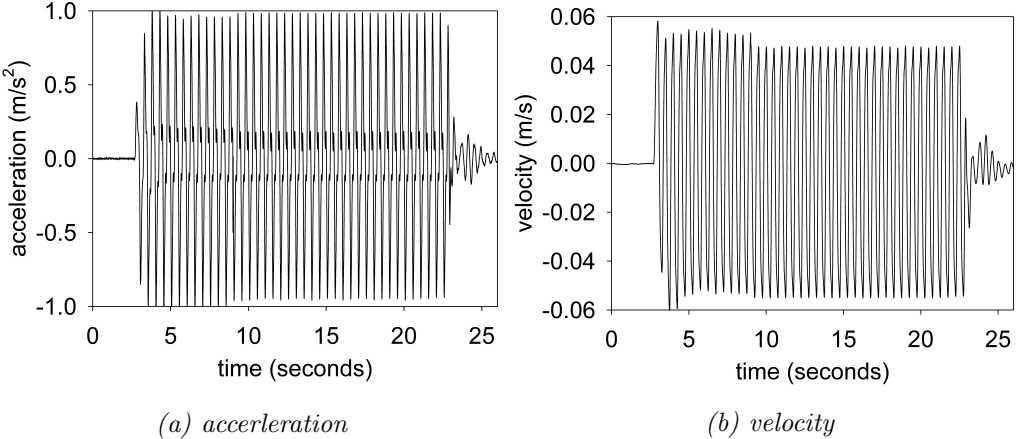


Figure 19: Ground acceleration profile, frequency of 2Hz and magnitude of 1g

598 In the final example, we perform numerical analysis of the earthquake
 599 induced submarine landslides. A plane strain model with the slope under
 600 water is shown in Figure 18. A 20m high slope with slope gradient of 45
 601 degrees is placed in a horizontal and vertical structure which was used to
 602 be a scaling table to apply earthquake loading. We simplify the earthquake
 603 loading by simulating the ground shaking for 20 seconds with the constant
 604 ground acceleration of 1g and a constant frequency of 2Hz (Figure 19a). The
 605 ground motion is applied in terms of velocity (Figure 19b). An earthquake
 606 of this magnitude is possible. For instance, in the case of the 2023 Turkey-
 607 Syria Earthquake, significant ground shaking with peak ground acceleration
 608 exceeding 1g was observed at numerous locations. This serves as an example
 609 of the practical occurrence of such high levels of ground acceleration during
 610 seismic events. To generate the seismic loading, the same method was used
 611 as presented in the previous numerical example.

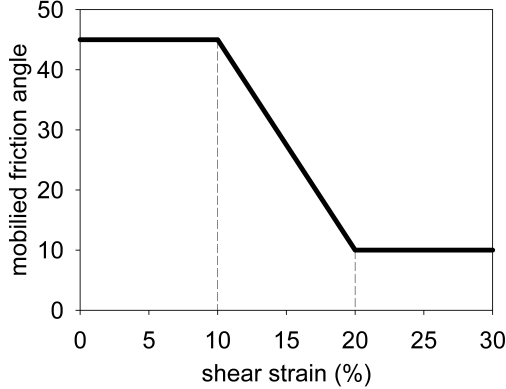


Figure 20: Mobilized friction angle in Mohr Coulomb model

612 A non-associated Mohr-Coulomb model is used for the soil. The soil grain
 613 has the density of 2650 kg/m^3 , Young's modulus of 10 kPa and Poisson's
 614 ratio of 0.3 and zero cohesion. The mobilized friction angle ϕ'_m is governed
 615 following the softening curve (see Figure 20) with the peak friction angle ϕ'_p
 616 of 45 degrees and the residual friction angle ϕ'_r of 10 degrees. The porosity
 617 is 0.3 and the average grain size of the soil is around $0.1 \mu\text{m}$ to mimic the
 618 undrained behavior. The mobilized dilatancy angle is calculated from the
 619 Rowe's stress dilatancy theory [36] as follow:

$$\sin \psi'_m = \frac{\sin \phi'_m - \sin \phi'_r}{1 - (\sin \phi'_r \sin \phi'_m)} \quad (100)$$

620 The solid plane is modeled as a rigid body acted as a shaking table. The
 621 contact between horizontal plane and the sand is the frictional contact with
 622 the friction coefficient of 0.1. No artificial damping is applied in the simu-
 623 lation. The contact between vertical plane and the sand is considered to be
 624 smooth with zero friction coefficient. On all boundary faces, the symmet-
 625 ric boundary condition is imposed, while the Neumann boundary condition
 626 is imposed at the top boundary for pressure ($d\rho/dx = 0 \text{ kPa}$) and density
 627 ($d\rho/dx = 0 \text{ kg/m}^3$). Symmetric boundary condition refers to a condition
 628 where the normal component of the velocity at the boundary face is set to
 629 zero, and the tangential component is equal to the tangential component of
 630 the neighboring cells. The mesh size is $0.25 \text{ m} \times 0.25 \text{ m}$ with 300852 element
 631 cells and 142316 material points. The simulation takes a couple of hours to
 632 perform 60 seconds of the simulation using 4096 CPUs.

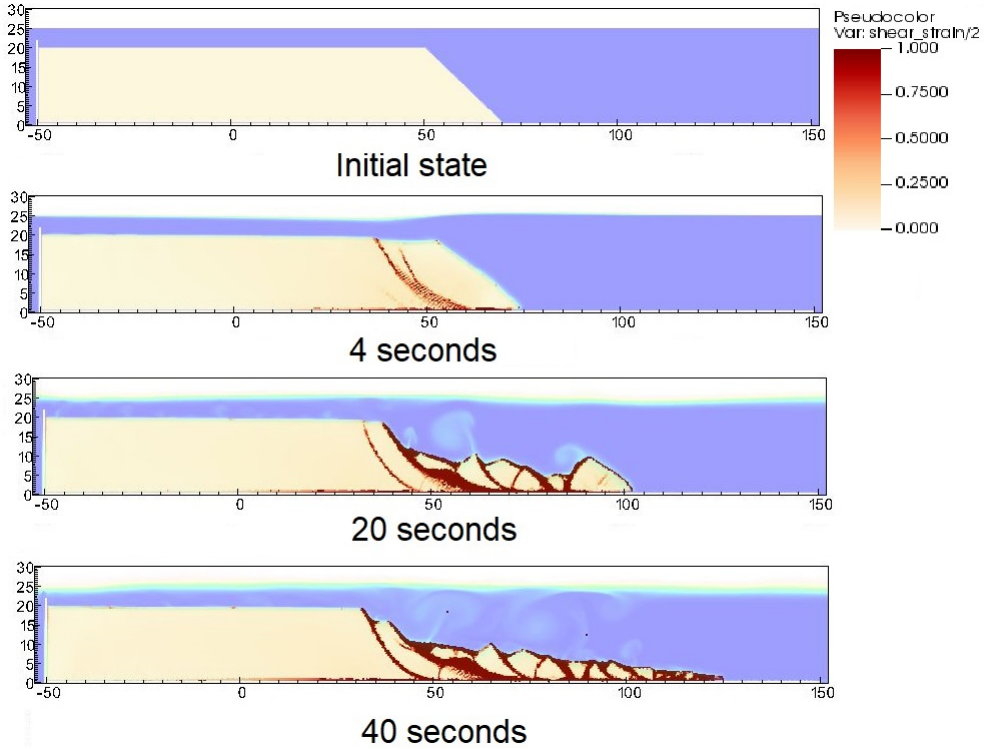


Figure 21: Shear strain during the earthquake-induced submarine landslides

633 We demonstrate the entire process and the mechanism of the earthquake-
 634 induced submarine landslides by showing the shear strain (Figure 21), the
 635 pore water pressure in atm (Figure 22) and the velocity (Figure 23). The
 636 failure mechanism can be characterized as the progressive failure mechanism.
 637 Here are some numerical observation:

- 638 1. At the initial of the seismic event, the seismic loading triggers the
 639 first slide at 3 seconds. At 4 seconds, the debris start to move with the
 640 maximum speed of around 2-3 m/s with multiple shear band developed
 641 in the slope. The wave generated from the submarine slide is around
 642 2-3 m towards the slide direction.

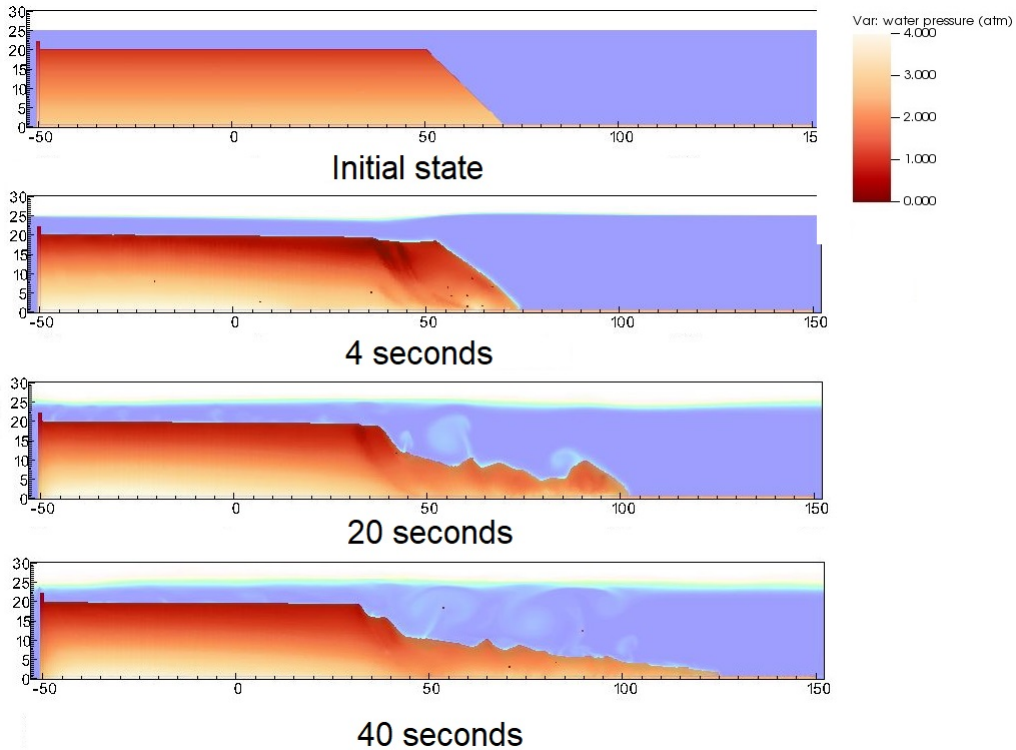


Figure 22: pore water pressure during the earthquake-induced submarine landslides

- 643 2. When the onset of the shear band occurs in the slope (for example
 644 at 4 seconds and 20 seconds), the negative excess pore water pressure
 645 is developed along this shear band with pore water pressure is under
 646 1atm. This is a typical dilatancy behavior when the soil is sheared
 647 rapidly in the undrained behavior.
- 648 3. When the seismic loading ends at 23 seconds, the last shear band is
 649 mobilized and the slope soon reaches to the final deposition. No more
 650 progressive failure developed in the slope. The turbulent flow developed
 651 as the interaction between debris flow and seawater.
- 652 Overall, we show the completed process of the earthquake-induced submarine
 653 landslides involving (1) earthquake triggering mechanism, (2) the onset of the
 654 shear band with the development of negative excess pore water pressure, (3)
 655 progressive failure mechanism, (4) submarine landslide induced wave to final
 656 deposition.

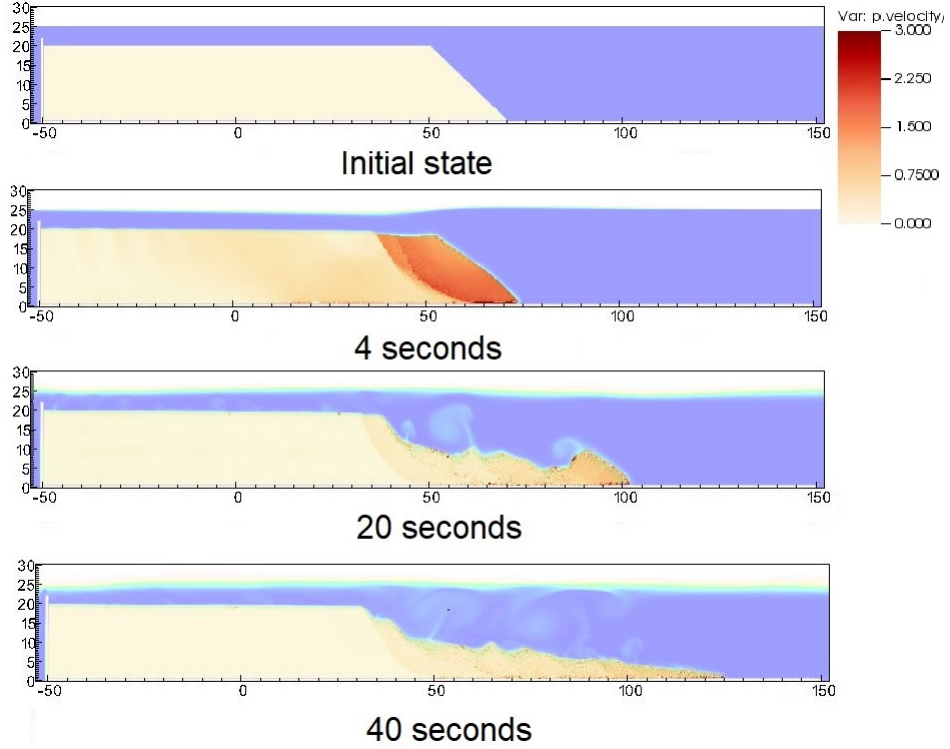


Figure 23: Velocity during the earthquake-induced submarine landslides

657 **Conclusions**

658 We have presented a numerical approach MPMICE for the simulation
 659 of large deformation soil-fluid-structure interaction, emphasizing the simu-
 660 lation of the earthquake-induced submarine landslides. The model uses (1)
 661 the Material Point Method for capturing the large deformation of iso-thermal
 662 porous media and solid structures and (2) Implicit Continuous Eulerian (com-
 663 pressible, conservative multi-material CFD formulation) for modeling the
 664 complex fluid flow including turbulence. This model is implemented in the
 665 high-performance Uintah computational framework and validated against an-
 666 alytical solution and experiment. We then demonstrate the capability of the
 667 model to simulate the entire process of the earthquake induced submarine
 668 landslides.

669 **Acknowledgements**

670 The authors gratefully acknowledge Dr. James Guilkey and Dr. Todd
 671 Harman from the University of Utah for sharing the insight on the theoretical
 672 framework of MPMICE which this work is based. This project has received
 673 funding from the European Union's Horizon 2020 research and innovation
 674 program under the Marie Skłodowska-Curie Actions (MSCA) Individual Fel-
 675 lowship (Project SUBSLIDE "Submarine landslides and their impacts on
 676 offshore infrastructures") grant agreement 101022007. The authors would
 677 also like to acknowledge the support from the Research Council of Norway
 678 through its Centers of Excellence funding scheme, project number 262644
 679 Porelab. The computations were performed on High Performance Comput-
 680 ing resources provided by UNINETT Sigma2 - the National Infrastructure
 681 for High Performance Computing and Data Storage in Norway.

682 **Appendix: Equation derivation**

683 Before deriving the governing equation, we define the Lagrangian deriva-
 684 tive for a state variable f as:

$$\frac{D_f f}{Dt} = \frac{\partial f}{\partial t} + \mathbf{U}_f \cdot \nabla f \quad \frac{D_s f}{Dt} = \frac{\partial f}{\partial t} + \mathbf{U}_s \cdot \nabla f \quad (101)$$

685 we use some definition following [22] as below:

$$-\frac{1}{V} \left[\frac{\partial V_f}{\partial p} \right] \equiv \kappa_f \quad \text{isothermal compressibility of fluid} \quad (102)$$

$$\frac{1}{V} \left[\frac{\partial V_f}{\partial T} \right] \equiv \alpha_f \quad \text{constant pressure thermal expansivity of fluid} \quad (103)$$

686 Then, the rate of volume with incompressible solid grains are calculated as
 687 belows:

$$\frac{1}{V} \frac{D_f V_f}{Dt} = \frac{1}{V} \left(\left[\frac{\partial V_f}{\partial p} \right] \frac{D_f P_{eq}}{Dt} + \left[\frac{\partial V_f}{\partial T_f} \right] \frac{D_f T_f}{Dt} \right) = \frac{1}{V} \left(-\kappa_f \frac{D_f P_{eq}}{Dt} + \alpha_f \frac{D_f T_f}{Dt} \right) \quad (104)$$

688 *Evolution of porosity*

689 Solving the solid mass balance equation (4) with the definition of solid
 690 mass in equation (2), it leads to the rate of porosity as belows:

$$\frac{D_s m_s}{Dt} = \frac{D_s (\phi_s \rho_s V)}{Dt} = \rho_s V \frac{D_s \phi_s}{Dt} + \phi_s V \frac{D_s \rho_s}{Dt} + \phi_s \rho_s \frac{D_s V}{Dt} = 0 \quad (105)$$

691 The soil grains are assumed to be incompressible, therefore, term 2 in the
 692 right hand side is zero. leading to:

$$V \frac{D_s \phi_s}{Dt} + \phi_s \frac{D_s V}{Dt} = 0 \quad (106)$$

693 Dividing all terms with V with the equation $\frac{1}{V} \frac{D_s V}{Dt} = \nabla \cdot \mathbf{U}_s$, it leads to:

$$\frac{D_s n}{Dt} = \frac{\partial n}{\partial t} + \mathbf{U}_s \cdot \nabla n = \phi_s \nabla \cdot \mathbf{U}_s \quad (107)$$

694 **Momentum conservation**

695 The linear momentum balance equations for the fluid phases based on
 696 mixture theory are:

$$\frac{1}{V} \frac{D_f(m_f \mathbf{U}_f)}{Dt} = \nabla \cdot (-\phi_f p_f \mathbf{I}) + \nabla \cdot \boldsymbol{\tau}_f + \bar{\rho}_f \mathbf{b} + \sum \mathbf{f}_d + \mathbf{f}_b \quad (108)$$

698 On the right hand sand, the first term is the divergence of partial fluid phase
 699 stress, the third term is the body force, the fourth term is the drag force
 700 (momentum exchange) and the fifth term is the buoyant force described in
 701 [37] for the immiscible mixtures. The buoyant force is in the form as belows:

$$\mathbf{f}_b = \boldsymbol{\sigma}_f \nabla(n) \quad (109)$$

702 As a result, the linear momentum balance equations for the fluid phases
 703 become as:

$$\frac{1}{V} \frac{D_f(m_f \mathbf{U}_f)}{Dt} = \frac{1}{V} \left[\frac{\partial(m_f \mathbf{U}_f)}{\partial t} + \nabla \cdot (m_f \mathbf{U}_f \mathbf{U}_f) \right] = -\phi_f \nabla p_f + \nabla \cdot \boldsymbol{\tau}_f + \bar{\rho}_f \mathbf{b} + \sum \mathbf{f}_d \quad (110)$$

704 The Reynolds stress component can be included in the term $\boldsymbol{\tau}_f$ to consider the
 705 turbulent effects if needed. To derive the linear momentum balance equation
 706 for the solid phase, we begin with the linear momentum balance equation for
 707 the mixture as:

$$\frac{1}{V} \frac{D_f(m_f \mathbf{U}_f)}{Dt} + \frac{1}{V} \frac{D_s(m_s \mathbf{U}_s)}{Dt} = \nabla \cdot (\boldsymbol{\sigma}) + \bar{\rho}_f \mathbf{b} + \bar{\rho}_s \mathbf{b} \quad (111)$$

708 Combining Terzaghi's equation (3) and subtracting both sides with equation
 709 (110), we obtain the linear momentum balance equations for the solid phase
 710 as:

$$\frac{1}{V} \frac{D_s(m_s \mathbf{U}_s)}{Dt} = \nabla \cdot (\boldsymbol{\sigma}') - \phi_s \nabla p_f + \bar{\rho}_s \mathbf{b} - \sum \mathbf{f}_d + \sum \mathbf{f}_{fric} \quad (112)$$

711 Here the \mathbf{f}_{fric} stems from the soil-structure interaction following the contact
 712 law between the soil/structure interfaces.

713 *Energy conservation*

714 We adopt the general form of the total energy balance equation for the
 715 porous media from [38], the total energy balance equations for the fluid phases
 716 are:

$$\frac{1}{V} \frac{D_f(m_f(e_f + 0.5\mathbf{U}_f^2))}{Dt} = \nabla \cdot (-np_f \mathbf{I}) \cdot \mathbf{U}_f + \nabla \cdot \mathbf{q}_f + (\bar{\rho}_f \mathbf{b}) \cdot \mathbf{U}_f + \sum \mathbf{f}_d \cdot \mathbf{U}_f + \sum q_{sf} \quad (113)$$

717 Applying the product rule $D(m\mathbf{U}^2) = D(m\mathbf{U} \cdot \mathbf{U}) = 2\mathbf{U} \cdot D(m\mathbf{U})$, the left
 718 hand side of equation (113) becomes:

719

$$\frac{1}{V} \frac{D_f(m_f(e_f + 0.5\mathbf{U}_f^2))}{Dt} = \frac{1}{V} \frac{D_f(m_f e_f)}{Dt} + \frac{1}{V} \frac{D_f(m_f \mathbf{U}_f)}{Dt} \cdot \mathbf{U}_f \quad (114)$$

720 Combining equations (110), (113), (114), we obtain the final form of the
 721 internal energy balance equation for the fluid phases as:

$$\frac{1}{V} \frac{D_f(m_f e_f)}{Dt} = \frac{1}{V} \left[\frac{\partial(m_f e_f)}{\partial t} + \nabla \cdot (m_f e_f \mathbf{U}_f) \right] = \bar{\rho}_f p_f \frac{D_f v_f}{Dt} + \nabla \cdot \mathbf{q}_f + \sum q_{sf} \quad (115)$$

722 On the right hand side, the terms include the average pressure-volume work,
 723 the average viscous dissipation, the thermal transport and the energy ex-
 724 change between solid and fluid respectively. The heat flux is $\mathbf{q}_f = \bar{\rho}_f \beta_f \nabla T_f$
 725 with β_f being the thermal conductivity coefficient. To derive the internal
 726 energy balance equation for the solid phase, we introduce the rate of the
 727 internal energy for the thermoelastic materials as a function of elastic strain
 728 tensor $\boldsymbol{\epsilon}_s^e$ and temperature T_s as belows:

$$\frac{m_s}{V} \frac{D_s(e_s)}{Dt} = \boldsymbol{\sigma}' : \frac{D_s(\boldsymbol{\epsilon}_s^e)}{Dt} + \frac{D_s(e_s)}{D_s(T_s)} \frac{D_s(T_s)}{Dt} = \boldsymbol{\sigma}' : \frac{D_s(\boldsymbol{\epsilon}_s^e)}{Dt} + c_v \frac{D_s(T_s)}{Dt} \quad (116)$$

729 c_v is the specific heat at the constant volume of the solid materials. The total
 730 energy balance equation for the mixture based on [38] can be written as:

731

$$\begin{aligned} \frac{1}{V} \frac{D_f(m_f(e_f + 0.5\mathbf{U}_f^2))}{Dt} + \frac{1}{V} \frac{D_s(m_s(e_s + 0.5\mathbf{U}_s^2))}{Dt} &= \nabla \cdot (-\phi_f p_f \mathbf{I}) \cdot \mathbf{U}_f \\ &+ \nabla \cdot (\boldsymbol{\sigma}' - \phi_s p_f \mathbf{I}) \cdot \mathbf{U}_s + (-\phi_f p_f \mathbf{I}) : \nabla \mathbf{U}_f + \boldsymbol{\sigma}' : \nabla \mathbf{U}_s \\ &+ (\bar{\rho}_f \mathbf{b}) \cdot \mathbf{U}_f + (\bar{\rho}_s \mathbf{b}) \cdot \mathbf{U}_s + \nabla \cdot \mathbf{q}_f + \nabla \cdot \mathbf{q}_s + \sum \mathbf{f}_d \cdot (\mathbf{U}_f - \mathbf{U}_s) \end{aligned} \quad (117)$$

⁷³² Subtracting equation (117), (116) to equations (113) and (112), we obtained
⁷³³ the internal energy balance equation for solid phase as:

$$\boldsymbol{\sigma}' : \frac{D_s(\epsilon_s^e)}{Dt} + \frac{m_s}{V} c_v \frac{D_s(T_s)}{Dt} = \Delta W_s + \Delta W_{friction} + \nabla \cdot \mathbf{q}_s - \sum q_{sf} \quad (118)$$

⁷³⁴ On the right hand side, the terms include the work rate from frictional sliding
⁷³⁵ between solid materials $\Delta W_{friction}$, thermal transport and energy exchange
⁷³⁶ between solid and fluid respectively. The heat flux is $\mathbf{q}_s = \bar{\rho}_s \beta_s \nabla T_s$ with β_s
⁷³⁷ being the thermal conductivity of the solid materials, the mechanical work
⁷³⁸ rate $\Delta W_s = \boldsymbol{\sigma}' : \frac{D_s(\epsilon_s)}{Dt} = \boldsymbol{\sigma}' : (\frac{D_s(\epsilon_s^e)}{Dt} + \frac{D_s(\epsilon_s^p)}{Dt})$ computed from the constitutive
⁷³⁹ model with ϵ_s^p is the plastic strain tensor, . By subtracting the term $\boldsymbol{\sigma}' : \frac{D_s(\epsilon_s^e)}{Dt}$,
⁷⁴⁰ we get the final form of the energy balance equation as:

$$\frac{m_s}{V} c_v \frac{D_s(T_s)}{Dt} = \boldsymbol{\sigma}' : \frac{D_s(\epsilon_s^p)}{Dt} + \Delta W_{friction} + \nabla \cdot \mathbf{q}_s - \sum q_{sf} \quad (119)$$

⁷⁴¹ Advanced Fluid Pressure

⁷⁴² The discretization of the pressure equation begins with the Lagrangian
⁷⁴³ cell face velocity and the equation for the pressure as:

$$\bar{\rho}_{f,FC} \frac{\mathbf{U}_{f,FC}^{n+1} - \mathbf{U}_{f,FC}^n}{dt} = n \nabla^{FC} P_{f,c}^{n+1} + \bar{\rho}_{f,FC} \mathbf{b} \quad (120)$$

⁷⁴⁴

$$\kappa \frac{dP}{dt} = \nabla^c \cdot \mathbf{U}_{f,FC}^{n+1} \quad (121)$$

⁷⁴⁵ The divergence of the equation (120) with $\nabla \cdot \mathbf{b} = 0$ is:

$$\nabla^c \cdot \mathbf{U}_{f,FC}^{n+1} - \nabla^c \cdot \mathbf{U}_{f,FC}^n = \nabla^c \frac{\Delta t}{\rho_{f,FC}^n} \cdot \nabla^{FC} (P_{f,c}^n + \Delta P_{f,c}^n) \quad (122)$$

⁷⁴⁶ To solve this equation, we define the cell face intermediate velocity $\mathbf{U}_{f,FC}^*$ as:

$$\bar{\rho}_{f,FC} \frac{\mathbf{U}_{f,FC}^* - \mathbf{U}_{f,FC}^n}{\Delta t} = n \nabla^{FC} P_{f,c}^n + \bar{\rho}_{f,FC} \mathbf{b} \quad (123)$$

⁷⁴⁷ The divergence of the equation (123) is:

$$\nabla^c \cdot \mathbf{U}_{f,FC}^* - \nabla^c \cdot \mathbf{U}_{f,FC}^n = \nabla^c \frac{\Delta t}{\rho_{f,FC}^n} \cdot \nabla^{FC} P_{f,c}^n \quad (124)$$

⁷⁴⁸ Combining equations (121, 122, 124), it leads to:

$$\left(\kappa - \nabla^c \frac{\Delta t}{\rho_{f,FC}^n} \cdot \nabla^{FC} \right) \Delta P_{fc}^n = -\nabla^c \cdot \mathbf{U}_{f,FC}^* \quad (125)$$

⁷⁴⁹ When the fluid is incompressible, κ approaches to zero and the equation
⁷⁵⁰ (125) becomes the Poisson's equation for the incompressible fluid flow.

⁷⁵¹ *Momentum and Energy exchange with an implicit solver*

⁷⁵² Considering the fluid momentum balance equation as:

$$(m\mathbf{U})_{f,FC}^{n+1} = (m\mathbf{U})_{f,FC}^n - \Delta t(Vn\nabla^{FC}P_{f,c}^n + m_f\mathbf{b}) + VK\Delta t(\mathbf{U}_{s,FC}^{n+1} - \mathbf{U}_{f,FC}^{n+1}) \quad (126)$$

⁷⁵³ And assuming $m_{f,FC}^{n+1} = m_{f,FC}^n$, we get:

$$\mathbf{U}_{f,FC}^{n+1} = \mathbf{U}_{f,FC}^n - \Delta t\left(\frac{\nabla^{FC}P_{fc}^n}{\rho_{f,FC}^n} + \mathbf{b}\right) + \frac{\Delta tK}{\bar{\rho}_{f,FC}^n}(\mathbf{U}_{s,FC}^{n+1} - \mathbf{U}_{f,FC}^{n+1}) \quad (127)$$

⁷⁵⁴ As defined in the section 'Advanced Fluid Pressure', the cell face intermediate
⁷⁵⁵ fluid velocity $\mathbf{U}_{f,FC}^* = \Delta t(\nabla^{FC}P_{fc}^n/\rho_{f,FC}^n + \mathbf{b})$ is computed as:

$$\mathbf{U}_{f,FC}^{n+1} = \mathbf{U}_{f,FC}^* + \frac{\Delta tK}{\bar{\rho}_{f,FC}^n}(\mathbf{U}_{s,FC}^{n+1} - \mathbf{U}_{f,FC}^{n+1}) \quad (128)$$

⁷⁵⁶ Considering the solid momentum balance equation as:

$$(m\mathbf{U})_{s,FC}^{n+1} = (m\mathbf{U})_{s,FC}^n - \Delta t(V\nabla^{FC} \cdot \boldsymbol{\sigma}'^n - V(1-n)\nabla^{FC}P_{f,c}^n + m_s\mathbf{b}) - VK\Delta t(\mathbf{U}_{s,FC}^{n+1} - \mathbf{U}_{f,FC}^{n+1}) \quad (129)$$

⁷⁵⁷ We define the cell face intermediate solid velocity as $\mathbf{U}_{s,FC}^* = \Delta t(\nabla^{FC} \cdot \boldsymbol{\sigma}'^n / \bar{\rho}_{s,FC}^n - \nabla^{FC}P_{f,c}^n / \rho_s + \mathbf{b})$ leading to:

$$\mathbf{U}_{s,FC}^{n+1} = \mathbf{U}_{s,FC}^* - \frac{\Delta tK}{\bar{\rho}_{s,FC}^n}(\mathbf{U}_{s,FC}^{n+1} - \mathbf{U}_{f,FC}^{n+1}) \quad (130)$$

⁷⁵⁹ Combining equation (128) and (130) we get:

$$\begin{aligned} \mathbf{U}_{f,FC}^* + \Delta\mathbf{U}_{f,FC} &= \mathbf{U}_{f,FC}^* + \frac{\Delta tK}{\bar{\rho}_{f,FC}^n}(\mathbf{U}_{s,FC}^* + \Delta\mathbf{U}_{s,FC} - \mathbf{U}_{f,FC}^* - \Delta\mathbf{U}_{f,FC}) \\ \mathbf{U}_{s,FC}^* + \Delta\mathbf{U}_{s,FC} &= \mathbf{U}_{s,FC}^* - \frac{\Delta tK}{\bar{\rho}_{s,FC}^n}(\mathbf{U}_{s,FC}^* + \Delta\mathbf{U}_{s,FC} - \mathbf{U}_{f,FC}^* - \Delta\mathbf{U}_{f,FC}) \end{aligned} \quad (131)$$

760 Rearranging the equation (131), it leads to the linear system of equations as
 761 belows:

$$\begin{vmatrix} (1 + \beta_{12,FC}) & -\beta_{12,FC} \\ -\beta_{21,FC} & (1 + \beta_{21,FC}) \end{vmatrix} \begin{vmatrix} \Delta \mathbf{U}_{f,FC} \\ \Delta \mathbf{U}_{s,FC} \end{vmatrix} = \begin{vmatrix} \beta_{12,FC} (\mathbf{U}_{s,FC}^* - \mathbf{U}_{f,FC}^*) \\ \beta_{21,FC} (\mathbf{U}_{f,FC}^* - \mathbf{U}_{s,FC}^*) \end{vmatrix}$$

762 Solving this linear equations with $\beta_{12,FC} = (\Delta t K) / \bar{\rho}_{f,FC}^n$ and $\beta_{21,FC} =$
 763 $(\Delta t K) / \bar{\rho}_{s,FC}^n$ with K is the momentum exchange coefficient. Similar deriva-
 764 tion can be performed to computed the cell-center velocity increment leading
 765 to:

$$\begin{vmatrix} (1 + \beta_{12c}) & -\beta_{12c} \\ -\beta_{21c} & (1 + \beta_{21c}) \end{vmatrix} \begin{vmatrix} \Delta \mathbf{U}_{f,c} \\ \Delta \mathbf{U}_{sc} \end{vmatrix} = \begin{vmatrix} \beta_{12c} (\mathbf{U}_{sc}^* - \mathbf{U}_{f,c}^*) \\ \beta_{21c} (\mathbf{U}_{f,c}^* - \mathbf{U}_{sc}^*) \end{vmatrix}$$

766 with $\beta_{12c} = (\Delta t K) / \bar{\rho}_{f,c}^n$ and $\beta_{21c} = (\Delta t K) / \bar{\rho}_{sc}^n$ and the cell-centered interme-
 767 diate velocity can be calculated by:

$$\begin{aligned} \mathbf{U}_{f,c}^* &= \mathbf{U}_{f,c}^n + \Delta t \left(-\frac{\nabla P_{f,c}^{n+1}}{\rho_{f,c}^n} + \frac{\nabla \cdot \boldsymbol{\tau}_{f,c}^n}{\bar{\rho}_{f,c}^n} + \mathbf{b} \right) \\ \mathbf{U}_{sc}^* &= \mathbf{U}_{sc}^n + \Delta t \left(\frac{\nabla \cdot \boldsymbol{\sigma}_c'^n}{\bar{\rho}_{sc}^n} - \frac{\nabla P_{f,c}^{n+1}}{\rho_s} + \mathbf{b} \right) \end{aligned} \quad (132)$$

768 For generalize multi materials i,j = 1:N, the linear equations is in the form
 769 as:

$$\begin{vmatrix} (1 + \beta_{ij}) & -\beta_{ij} \\ -\beta_{ji} & (1 + \beta_{ji}) \end{vmatrix} \begin{vmatrix} \Delta \mathbf{U}_i \\ \Delta \mathbf{U}_j \end{vmatrix} = \begin{vmatrix} \beta_{ij} (\mathbf{U}_i^* - \mathbf{U}_j^*) \\ \beta_{ji} (\mathbf{U}_j^* - \mathbf{U}_i^*) \end{vmatrix}$$

770 Similar approach applied for the ernergy exchange term leading to:

$$\begin{vmatrix} (1 + \eta_{ij}) & -\eta_{ij} \\ -\eta_{ji} & (1 + \eta_{ji}) \end{vmatrix} \begin{vmatrix} \Delta T_i \\ \Delta T_j \end{vmatrix} = \begin{vmatrix} \eta_{ij} (T_i^n - T_j^n) \\ \eta_{ji} (T_j^n - T_i^n) \end{vmatrix}$$

771 with η is the energy exchange coefficient.

772 References

- 773 [1] D. Yuk, S. Yim, P.-F. Liu, Numerical modeling of submarine mass-
 774 movement generated waves using RANS model, Computers and Geo-
 775 sciences 32 (7) (2006) 927–935. doi:10.1016/j.cageo.2005.10.028.
 776 URL <https://doi.org/10.1016/j.cageo.2005.10.028>

- 777 [2] S. Glimsdal, J.-S. L'Heureux, C. B. Harbitz, F. Løvholt, The 29th january 2014 submarine landslide at statland, norway—landslide dynamics,
778 tsunami generation, and run-up, *Landslides* 13 (6) (2016) 1435–1444.
779 doi:10.1007/s10346-016-0758-7.
780 URL <https://doi.org/10.1007/s10346-016-0758-7>
- 782 [3] S. Abadie, D. Morichon, S. Grilli, S. Glockner, Numerical simulation
783 of waves generated by landslides using a multiple-fluid navier–stokes model,
784 *Coastal Engineering* 57 (9) (2010) 779–794.
785 doi:10.1016/j.coastaleng.2010.03.003.
786 URL <https://doi.org/10.1016/j.coastaleng.2010.03.003>
- 787 [4] M. Rauter, S. Viroulet, S. S. Gylfadóttir, W. Fellin, F. Løvholt, Granular
788 porous landslide tsunami modelling – the 2014 lake askja flank collapse,
789 *Nature Communications* 13 (1) (Feb. 2022). doi:10.1038/s41467-022-
790 28296-7.
791 URL <https://doi.org/10.1038/s41467-022-28296-7>
- 792 [5] Q.-A. Tran, W. Sołowski, Generalized interpolation material point
793 method modelling of large deformation problems including strain-
794 rate effects – application to penetration and progressive fail-
795 ure problems, *Computers and Geotechnics* 106 (2019) 249–265.
796 doi:10.1016/j.compgeo.2018.10.020.
797 URL <https://doi.org/10.1016/j.compgeo.2018.10.020>
- 798 [6] T. Capone, A. Panizzo, J. J. Monaghan, SPH modelling of water
799 waves generated by submarine landslides, *Journal of Hydraulic Research*
800 48 (sup1) (2010) 80–84. doi:10.1080/00221686.2010.9641248.
801 URL <https://doi.org/10.1080/00221686.2010.9641248>
- 802 [7] X. Zhang, E. Oñate, S. A. G. Torres, J. Bleyer, K. Krabbenhoft, A
803 unified lagrangian formulation for solid and fluid dynamics and its pos-
804 sibility for modelling submarine landslides and their consequences, *Com-
805 puter Methods in Applied Mechanics and Engineering* 343 (2019) 314–
806 338. doi:10.1016/j.cma.2018.07.043.
807 URL <https://doi.org/10.1016/j.cma.2018.07.043>
- 808 [8] R. Dey, B. C. Hawlader, R. Phillips, K. Soga, Numerical modelling
809 of submarine landslides with sensitive clay layers, *Géotechnique* 66 (6)

- 810 (2016) 454–468. doi:10.1680/jgeot.15.p.111.
811 URL <https://doi.org/10.1680/jgeot.15.p.111>
- 812 [9] S. Bandara, K. Soga, Coupling of soil deformation and pore fluid flow
813 using material point method, *Computers and Geotechnics* 63 (2015)
814 199–214. doi:10.1016/j.compgeo.2014.09.009.
815 URL <https://doi.org/10.1016/j.compgeo.2014.09.009>
- 816 [10] A. P. Tampubolon, T. Gast, G. Klár, C. Fu, J. Teran, C. Jiang,
817 K. Museth, Multi-species simulation of porous sand and water
818 mixtures, *ACM Transactions on Graphics* 36 (4) (2017) 1–11.
819 doi:10.1145/3072959.3073651.
820 URL <https://doi.org/10.1145/3072959.3073651>
- 821 [11] A. S. Baumgarten, K. Kamrin, A general constitutive model for dense,
822 fine-particle suspensions validated in many geometries, *Proceedings*
823 of the National Academy of Sciences 116 (42) (2019) 20828–20836.
824 doi:10.1073/pnas.1908065116.
825 URL <https://doi.org/10.1073/pnas.1908065116>
- 826 [12] Q.-A. Tran, W. Sołowski, Temporal and null-space filter for the ma-
827 terial point method, *International Journal for Numerical Methods in*
828 *Engineering* 120 (3) (2019) 328–360. doi:10.1002/nme.6138.
829 URL <https://doi.org/10.1002/nme.6138>
- 830 [13] X. Zheng, F. Pisanò, P. J. Vardon, M. A. Hicks, An explicit stabilised
831 material point method for coupled hydromechanical problems in two-
832 phase porous media, *Computers and Geotechnics* 135 (2021) 104112.
833 doi:10.1016/j.compgeo.2021.104112.
834 URL <https://doi.org/10.1016/j.compgeo.2021.104112>
- 835 [14] Q. A. Tran, W. Sołowski, M. Berzins, J. Guilkey, A convected particle
836 least square interpolation material point method, *International Jour-
837 nal for Numerical Methods in Engineering* 121 (6) (2019) 1068–1100.
838 doi:10.1002/nme.6257.
839 URL <https://doi.org/10.1002/nme.6257>
- 840 [15] J. Zhao, T. Shan, Coupled cfd–dem simulation of fluid–particle in-
841 teraction in geomechanics, *Powder Technology* 239 (2013) 248–258.

- 842 doi:<https://doi.org/10.1016/j.powtec.2013.02.003>.
843 URL <https://www.sciencedirect.com/science/article/pii/S0032591013001113>
- 844 [16] T. Shan, J. Zhao, A coupled cfd-dem analysis of granular flow im-
845 impacting on a water reservoir, *Acta Mechanica* 225 (2014) 2449–2470.
846 doi:<https://doi.org/10.1007/s00707-014-1119-z>.
- 847 [17] S. Zhao, J. Zhao, W. Liang, F. Niu, Multiscale modeling of coupled
848 thermo-mechanical behavior of granular media in large deforma-
849 tion and flow, *Computers and Geotechnics* 149 (2022) 104855.
850 doi:<https://doi.org/10.1016/j.compgeo.2022.104855>.
851 URL <https://www.sciencedirect.com/science/article/pii/S0266352X22002038>
- 852 [18] S. Zhao, H. Chen, J. Zhao, Multiscale modeling of freeze-thaw be-
853 havior in granular media, *Acta Mechanica Sinica* 37 (2023) 722195.
854 doi:<https://doi.org/10.1007/s10409-022-22195-x>.
- 855 [19] N. M. Pinyol, M. Alvarado, E. E. Alonso, F. Zabala,
856 Thermal effects in landslide mobility, *Géotechnique* 68 (6)
857 (2018) 528–545. arXiv:<https://doi.org/10.1680/jgeot.17.P.054>,
858 doi:[10.1680/jgeot.17.P.054](https://doi.org/10.1680/jgeot.17.P.054).
859 URL <https://doi.org/10.1680/jgeot.17.P.054>
- 860 [20] J.-S. Chen, M. Hillman, S.-W. Chi, Meshfree methods: Progress made
861 after 20 years, *Journal of Engineering Mechanics* 143 (4) (Apr. 2017).
862 doi:[10.1061/\(asce\)em.1943-7889.0001176](https://doi.org/10.1061/(asce)em.1943-7889.0001176).
863 URL [https://doi.org/10.1061/\(asce\)em.1943-7889.0001176](https://doi.org/10.1061/(asce)em.1943-7889.0001176)
- 864 [21] F. H. Harlow, A. A. Amsden, Numerical calculation of almost incom-
865 pressible flow, *Journal of Computational Physics* 3 (1) (1968) 80–93.
866 doi:[https://doi.org/10.1016/0021-9991\(68\)90007-7](https://doi.org/10.1016/0021-9991(68)90007-7).
867 URL <https://www.sciencedirect.com/science/article/pii/0021999168900077>
- 868 [22] B. A. Kashiwa, A multifield model and method for fluid-structure in-
869 teraction dynamics, Tech. Rep. LA-UR-01-1136, Los Alamos National
870 Laboratory (2001).
- 871 [23] J. Guilkey, T. Harman, B. Banerjee, An eulerian-lagrangian
872 approach for simulating explosions of energetic devices,
873 *Computers and Structures* 85 (11) (2007) 660 – 674.

- 874 doi:<https://doi.org/10.1016/j.compstruc.2007.01.031>.
875 URL <http://www.sciencedirect.com/science/article/pii/S0045794907000429>
- 876 [24] A. S. Baumgarten, B. L. Couchman, K. Kamrin, A coupled finite volume
877 and material point method for two-phase simulation of liquid–sediment
878 and gas–sediment flows, Computer Methods in Applied Mechanics and
879 Engineering 384 (2021) 113940. doi:[10.1016/j.cma.2021.113940](https://doi.org/10.1016/j.cma.2021.113940).
880 URL <https://doi.org/10.1016/j.cma.2021.113940>
- 881 [25] J. Clausen, L. Damkilde, L. Andersen, Efficient return algorithms for
882 associated plasticity with multiple yield planes, International Journal
883 for Numerical Methods in Engineering 66 (6) (2006) 1036–1059.
884 arXiv:<https://onlinelibrary.wiley.com/doi/pdf/10.1002/nme.1595>,
885 doi:<https://doi.org/10.1002/nme.1595>.
886 URL <https://onlinelibrary.wiley.com/doi/abs/10.1002/nme.1595>
- 887 [26] P. Moin, K. Squires, W. Cabot, S. Lee, A dynamic
888 subgrid-scale model for compressible turbulence and scalar
889 transport, Physics of Fluids A: Fluid Dynamics 3 (11)
890 (1991) 2746–2757. arXiv:https://pubs.aip.org/aip/pof/article-pdf/3/11/2746/12328150/2746_1_online.pdf, doi:[10.1063/1.858164](https://doi.org/10.1063/1.858164).
891 URL <https://doi.org/10.1063/1.858164>
- 892 [27] S. Bardenhagen, J. Guilkey, K. Roessig, J. Brackbill, W. Witzel,
893 J.C.Foster, An improved contact algorithm for the material point
894 method and application to stress propagation in granular material,
895 CMES-Computer Modeling in Engineering and Sciences 2 (2001) 509–
896 522. doi:[10.3970/cmes.2001.002.509](https://doi.org/10.3970/cmes.2001.002.509).
- 897 [28] J. A. M. K. R. Beetstra, M. A. van der Hoef, Drag force of intermediate
898 reynolds number flow past mono- and bidisperse arrays of spheres,
899 Fluid Mechanics and Transport Phenomena 53 (2) (2007) 489 – 501.
900 doi:<https://doi.org/10.1002/aic.11065>.
- 901 [29] R. W. Stewart, The air-sea momentum exchange, Boundary-Layer Me-
902 teorology 6 (1-2) (1974) 151–167. doi:[10.1007/bf00232481](https://doi.org/10.1007/bf00232481).
903 URL <https://doi.org/10.1007/bf00232481>
- 904 [30] S. G. Bardenhagen, E. M. Kober, The generalized interpolation material
905 point method, Computer Modeling in Engineering and Sciences 5 (2004)
- 906

- 907 477–496. doi:10.1016/j.compgeo.2021.104199.
 908 URL <https://doi.org/10.3970/cmes.2004.005.477>
- 909 [31] S. G. Amiri, E. Taheri, A. Lavasan, A hybrid finite element model for
 910 non-isothermal two-phase flow in deformable porous media, Computers
 911 and Geotechnics 135 (2021) 104199. doi:10.1016/j.compgeo.2021.104199.
 912 URL <https://doi.org/10.1016/j.compgeo.2021.104199>
- 913 [32] S. A. R. C. Mariotti, P. Heinrich, Numerical simulation of sub-
 914 marine landslides and their hydraulic effects, Journal of Waterway,
 915 Port, Coastal, and Ocean Engineering 123 (4) (1997).
 916 doi:[https://doi.org/10.1061/\(ASCE\)0733-950X\(1997\)123:4\(149\)](https://doi.org/10.1061/(ASCE)0733-950X(1997)123:4(149)).
- 917 [33] A. Alsardi, A. Yerro, Runout Modeling of Earthquake-Triggered
 918 Landslides with the Material Point Method, pp. 21–31.
 919 arXiv:<https://ascelibrary.org/doi/pdf/10.1061/9780784483428.003>,
 920 doi:10.1061/9780784483428.003.
 921 URL <https://ascelibrary.org/doi/abs/10.1061/9780784483428.003>
- 922 [34] H. N., O. A., B. H. H., R. P., R. Fukagawa, Seismic slope failuremod-
 923 elling using the mesh-free sph method, International Journal of Geomate
 924 (2013) 660–665.
- 925 [35] T. Bhandari, F. Hamad, C. Moormann, K. Sharma,
 926 B. Westrich, Numerical modelling of seismic slope failure us-
 927 ing mpm, Computers and Geotechnics 75 (2016) 126–134.
 928 doi:<https://doi.org/10.1016/j.compgeo.2016.01.017>.
 929 URL <https://www.sciencedirect.com/science/article/pii/S0266352X16000264>
- 930 [36] D. Muir Wood, Soil behaviour and critical state soil mechanics, Cam-
 931 bridge University Press, United Kingdom, 1990.
- 932 [37] D. Drumheller, On theories for reacting immiscible mixtures, Inter-
 933 national Journal of Engineering Science 38 (3) (2000) 347 – 382.
 934 doi:[https://doi.org/10.1016/S0020-7225\(99\)00047-6](https://doi.org/10.1016/S0020-7225(99)00047-6).
 935 URL <http://www.sciencedirect.com/science/article/pii/S0020722599000476>
- 936 [38] S. Hassanizadeh, Derivation of basic equations of mass transport in
 937 porous media, part1: Macroscopic balance laws, Advances in Wa-
 938 ter Resources 9 (1986) 196–206. doi:[https://doi.org/10.1016/0309-1708\(86\)90024-2](https://doi.org/10.1016/0309-1708(86)90024-2).